U.PORTO
FEUP FACULDADE DE ENGENHARIA
UNIVERSIDADE DO PORTO

M 2025

OPTIMIZATION OF INCONEL 718 CLADDINGS FOR HIGH PERFORMANCE VIA WIRE LASER ADDITIVE MANUFACTURING

CARLOS DIOGO COELHO MOTA
MASTER'S DEGREE DISSERTATION IN MATERIALS ENGINEERING SUBMITTED TO THE FACULTY OF ENGINEERING OF UNIVERSITY OF PORTO

MANUEL FERNANDO GONÇALVES VIEIRA
SUPERVISOR
FULL PROFESSOR AT THE DEPARTMENT OF MECHANICAL ENGINEERING

CANDIDATO	Carlos Diogo Coelho Mota	*CÓDIGO*	201908011
TÍTULO	Optimization of Inconel 718 claddings for high performance via wire laser additive manufacturing		
DATA	25-07-2025		
LOCAL	Faculdade de Engenharia da Universidade do Porto – Sala F106 -		

JÚRI	*Presidente*	Sónia Luísa dos Santos Simões	DEMec/FEUP
	Arguente	Rui Ricardo Loureiro Amaral	INEGI
	Orientador	Manuel Fernando Gonçalves Vieira	DEMec/FEUP

"If we knew what it was we were doing, it would not be called research, would it?"

Albert Einstein

Abstract

In the context of Industry 4.0, additive manufacturing techniques have emerged as pivotal technologies, enabling the production of complex components with significant material savings and functional optimization. This thesis investigates the optimization of Inconel 718 clads deposited via Wire Laser Additive Manufacturing (WLAM) onto structural steel, S355 and stainless steel, 304L, aiming to enhance their mechanical and metallurgical properties for demanding applications. Comprehensive parameter optimization was carried out, examining the influence of laser power, wire feed rate, laser speed, and shielding gas pressure on dilution, wettability, porosity, and cracking.

Optimal deposition parameters were identified as 8.5 kW laser power, 0.55 m/min laser speed, 5 m/min wire feed rate, and 2 bar argon pressure for 304L stainless steel substrates, and 9.6 kW laser power, 0.6 m/min laser speed, 4.9 m/min wire feed rate, and 4 bar argon for S355 structural steel substrates. These parameters led to the clads with the least defects and having good wettability and dilution on the substrate.

Heat treatments, consisting of homogenization at 1200°C followed by a double aging cycle, significantly improved the mechanical performance of clads, increasing hardness from approximately 225 HV in as-built conditions to 412 HV post-treatment, representing an 84% improvement. Tensile tests further validated these benefits, showing remarkable enhancements in yield strength (from 447 MPa to 853 MPa horizontally, and from 488 MPa to 960 MPa vertically) and ultimate tensile strength (from 824 MPa to 1057 MPa horizontally, and from 836 MPa to 1090 MPa vertically) after heat treatment. Additionally, the applied heat treatment effectively reduced the hardness and brittleness of the Heat-Affected Zone (HAZ), resolving issues caused by microstructural transformations during deposition. Substantial mechanical anisotropy was observed, the vertical direction showed 38% elongation in the as-built state and 22% when heat treated, while the diagonal orientation had the lowest values at 28% and 14%, respectively. The highest elongation was observed in the as-built state at 41% and 25% after heat treatment, emphasizing the critical role of grain orientation on mechanical behaviour.

These findings offer significant practical implications, especially for high end industrial applications like aerospace, nuclear, energy generation, and chemical processing sectors, by substantially improving component reliability and extending operational lifespan.

Resumo

No contexto da Indústria 4.0, as técnicas de fabrico aditivo surgiram como tecnologias fundamentais, permitindo a produção de componentes complexos com uma significativa economia de material e otimização funcional. Esta dissertação investiga a otimização de revestimentos de Inconel 718 depositados por *Wire Laser Additive Manufacturing* sobre aço estrutural S355 e aço inoxidável 304L, com o objetivo de melhoria de propriedades mecânicas e metalúrgicas para aplicação em condições de maior exigência. Foi realizada uma optimização abrangente dos parâmetros, analisando a influência da potência do laser, da taxa de alimentação do fio, da do laser e da pressão do gás de proteção na diluição, molhabilidade, porosidade e fissuração.

Os parâmetros de deposição com melhores resultados foram: 8,5 kW de potência do laser, 0,55 m/min de velocidade do laser, 5 m/min de alimentação do fio e 2 bar de pressão de árgon para os substratos de aço inoxidável 304L; e 9,6 kW de potência do laser, 0,6 m/min de velocidade do laser, 4,9 m/min de alimentação do fio e 4 bar de árgon para os substratos de aço estrutural S355. Estes parâmetros resultaram em revestimentos com o mínimo de defeitos, boa molhabilidade e diluição adequada com o substrato.

Os tratamentos térmicos, consistindo numa homogeneização a 1200°C seguida de um ciclo duplo de envelhecimento, melhoraram significativamente o desempenho mecânico dos revestimentos, aumentando a dureza em aproximadamente 225 HV no estado *as-built* para 412 HV após o tratamento, representando uma melhoria de 84% na dureza. Os resultados dos ensaios de tração, evidenciaram um aumento dos valores de $R_{p0,2}$ de 447 MPa para 853 MPa na orientação horizontal e de 488 MPa para 960 MPa na orientação vertical e no R_m de 824 MPa para 1057 MPa na horizontal e de 836 MPa para 1090 MPa na vertical, sem e com tratamento térmico, respetivamente. Adicionalmente, o tratamento térmico aplicado reduziu eficazmente a dureza da Zona Termicamente Afetada (ZTA), diminuindo problemas relacionados com transformações microestruturais durante a deposição. Foi observada uma anisotropia mecânica substancial: a direção vertical apresentou 38% de alongamento no estado *as-built* e 22% após tratamento térmico, enquanto a orientação diagonal apresentou os valores mais baixos, com 28% e 14%, respetivamente. O maior alongamento foi registado no estado *as-built*, com 41%, e 25% após tratamento térmico, enfatizando o papel crítico da orientação dos grãos no comportamento mecânico.

Estes resultados têm implicações práticas significativas, especialmente para aplicações industriais de elevado desempenho, como os sectores aeroespaciais, nuclear, de geração de energia e de processamento químico, ao melhorar substancialmente a fiabilidade dos componentes e prolongar a sua vida útil operacional.

Acknowledgements

I would like to express my gratitude to everyone that helps in the development of this thesis. Firstly, I would like to thank my supervisor, Prof. Manuel Vieira, for his guidance and encouragement throughout not only the course of this research, but also the whole degree. Your expertise and insights have been invaluable in shaping this thesis and my university journey. I would like to extend this thanks to all the professors, technicians, and collaborators of the Metallurgical and Materials Engineering Department (DEMM) that have made this journey so meaningful and rewarding.

To Dr. André Ferreira, for giving me the opportunity to work on this theme with high industrial and scientific relevance. Also, for your knowledge and support that helped me in the elaboration of this thesis.

To all my friends throughout my degree made these years the most enjoyable of my life.

To Dr. Aida Moreira who made me grow fond of scientific research, and since then been a partner in most projects I have worked on.

Finally, I want to express my gratitude to my family and most importantly my parents, who always supported me. I am forever indebted to you. You made it possible for me to be here, by always giving me all the help and conditions I could ask for, and specially for still sticking up for me during the times my confidence was wavering. You mean everything to me.

Institutional Acknowledgments

I would like to express my sincere gratitude to IREPA LASER for presenting me the challenge that resulted in this thesis, and giving me all the material, information and support needed.

My appreciation goes to the Department of Mechanical Engineering (DEMec) for providing the essential equipment needed for the metallographic preparation, macrostructural and microstructural analysis, SEM/EDS analysis and tensile tests.

I also want to thank CINFU for the machining of the tensile specimens and INEGI for conducting the tensile tests.

Table of Contents

List of Figures

List of Tables

List of Abbreviations

A	Ultimate tensile strength
AM	Additive manufacturing
DED	Direct energy deposition
EBSD	Electron backscatter diffraction
EDS	Energy dispersive X-ray spectroscopy
HAZ	Heat-affected zone
R_m	Engineering ultimate strength
$R_{p0.2}$	0.2% Offset engineering yield strength
S	Structural steel
SEM	Scanning electron microscopy
SS	Stainless steel
WLAM	Wire laser additive manufacturing

1. Introduction

The ongoing advancements in industrial manufacturing, driven by the rapid progression of the Fourth Industrial Revolution (Industry 4.0), have significantly increased the demand for enhanced engineering materials. This transformation has led to the development of more efficient and faster manufacturing techniques to meet modern industry requirements. Additive Manufacturing (AM) has emerged as a crucial and robust fabrication method, evolving from 3D printing to enable the layer-by-layer deposition of similar or dissimilar materials [1].

Wire laser additive manufacturing (WLAM) is a flexible and fast manufacturing method used to product variants of high geometric complexity. This method uses the laser as a heat source to form a small melt pool on the substrate surface or a previously deposited layer, and then the metallic wire is delivered. Due to the relative movement of the substrate and the laser, the clad solidifies and forms a strong bond with the original surface. This manufacturing process of metal components is noted for the high energy density and low heat input, small thermal deformation of the workpiece, fast heating and cooling speed, the small grain size of the formed part, and easy to realize automation and intelligence. Making it possible to efficiently build large expensive metal components with complex geometry via WLAM [2-5].

The application of Inconel 718 as a cladding material or as a deposited layer via additive manufacturing techniques, such as WLAM, onto stainless steels or structural steels, has garnered significant interest in recent years. This approach combines the superior surface properties of nickel-based superalloys with the economic and mechanical advantages of more common structural metals. Inconel 718, a precipitation-hardenable nickel-chromium alloy, is well known for its high strength, excellent resistance to oxidation and corrosion, and remarkable performance at elevated temperatures, typically up to 700°C. These properties make it a suitable candidate for applications in aerospace, nuclear, and chemical processing industries, where components are exposed to aggressive environments [5,6].

Cladding Inconel 718 onto austenitic stainless steels such as 304L allows for significant cost reduction compared to producing full components from Inconel. While 304L exhibits good corrosion resistance and weldability, its performance under high-temperature and high-stress conditions is limited. Similarly, carbon steels such as S355 are widely used due to their excellent mechanical strength and low cost but lack the corrosion and thermal resistance required in many critical environments. By depositing a functional layer of Inconel 718 only where it is needed—typically at the surface exposed to harsh conditions—it is possible to enhance the service life of components without incurring the full cost of using high-performance alloys throughout the entire part [7,8].

This dissertation was developed in fulfilment of the requirements for the degree of Master of Science in Materials Engineering at the Faculty of Engineering of the University of Porto (FEUP) with the goal of an optimization of the Inconel 718 WLAM process.

1.1 Objectives and Document Organization

This work was conducted to achieve an optimization of the process parameters of Inconel 718 clads deposited on stainless steel 304L and structural steel S355, produced by Wire Laser Additive Manufacturing for IREPA LASER, through characterization of clads produced with a wide range of inputs. Furthermore, heat treatments for WLAM Inconel 718were studied.

The present document, entitled “Optimization of Inconel 718 Claddings for High Performance via Wire Laser Additive Manufacturing”, is structured into the following five chapters:

- **Chapter 1 (Introduction):** Presents the motivation, research objectives and dissertation framework.
- **Chapter 2 (Literature Review):** Provides an overview of the relevant literature for the work, focusing on the topics of wire laser additive manufacturing, cladding, heat treatments and process optimizations.
- **Chapter 3 (Methodology):** Describes, in detail, the followed methodology to achieve the goals set for each part of the thesis.
- **Chapter 4 (Results and Discussion):** Presents the findings from each part of the thesis and evaluates the obtained results, aiming at answering the main goals of the work.
- **Chapter 5 (Conclusions):** Summarizes the key findings of each part and suggests directions for future research that could be conducted.

2. Literature Review

Additive Manufacturing (AM) encompasses a diverse range of layer-by-layer fabrication techniques that construct physical parts directly from digital 3D models. Unlike traditional manufacturing methods, subtractive or formative, AM builds objects by depositing material only where needed, resulting in minimal waste and enabling the creation of complex geometries and optimized internal structures that are often impossible with conventional techniques [9,10]. The process typically begins with a CAD model, which is digitally sliced into layers and converted into a set of toolpaths for the printer to follow. A wide variety of materials can be processed through AM, including polymers, metals, ceramics, composites, and biomaterials, depending on the specific technique used [11].

AM has gained considerable attention due to its advantages in design freedom, mass customization, reduced material consumption, and rapid prototyping. These features have made AM an enabling technology in sectors such as aerospace, biomedical, automotive, and construction, where highly specialized, lightweight, and performance-critical components are required [10,12]. In the aerospace industry, for example, AM allows the fabrication of lightweight structures with integrated functionality, reducing both component count and weight. In the biomedical field, it enables patient-specific implants and scaffolds that conform exactly to anatomical data, improving clinical outcomes [13]. Moreover, the ability to produce parts on demand and locally supports decentralized manufacturing, reducing logistics costs and lead times—an asset in defence, space, and remote field operations [14].

In addition to functional and logistical benefits, AM offers environmental advantages. Its material efficiency and the possibility of using recyclable feedstocks contribute to a lower environmental footprint, especially when compared to subtractive manufacturing for low-volume or complex components [9,15]. Nonetheless, challenges remain. AM often requires significant post-processing to meet industrial tolerances and may suffer from high energy consumption, particularly in metal-based processes like directed energy deposition [16]. Material availability and qualification are also concerns for industrial scaling, along with ensuring repeatability and part certification. To overcome these issues, research is focused on process optimization, *in-situ* monitoring, machine learning integration, and the development of hybrid manufacturing systems that combine the strengths of AM with traditional techniques [17].

2.1 Direct Energy Deposition

Direct Energy Deposition (DED) is a versatile additive manufacturing method that enables the fabrication, repair, and surface enhancement of components by melting and depositing material feedstock—commonly powder or wire—into a localized melt pool using focused thermal energy. This heating can be achieved via high-power lasers, electron beams, or plasma arcs, and the material is added in a layer-by-layer fashion, allowing the creation of complex geometries and tailored microstructures that are unattainable with conventional subtractive or forming methods [18,19]. In contrast to Powder Bed Fusion

(PBF), which relies on a static powder bed and is typically constrained by build volume, DED offers pronounced geometric liberty and excels at large-scale part production, component repair, or hybrid manufacturing—making it essential for demanding sectors such as aerospace, energy, defence, and tooling where bespoke repair and part longevity are required [18,20].

A critical strength of DED lies in its compatibility with multi-axis robotic systems or CNC platforms, enabling deposition on curved or previously manufactured surfaces—a decisive edge in repair or augmentative manufacturing operations [20,21]. The process is influenced by a complex interplay of parameters, including laser or beam power, spot size, scanning path strategy, feed rate, travel speed, interlayer dwell, and cooling protocol. These interdependent variables govern melt-pool thermodynamics, solidification kinetics, and resultant microstructures—ultimately shaping mechanical characteristics, porosity, and residual stresses [19,22,23].

Recent efforts in multi-fidelity modelling combine high-fidelity thermal and melt-pool simulations with data-driven surrogates such as Gaussian-process regression to achieve accurate yet computationally efficient process maps [24]. In parallel, machine learning (ML) algorithms—including recurrent neural networks (RNN), long short-term memory (LSTM), and XGBoost—are being trained on sensor-derived data to predict melt-pool conditions in real time, enabling proactive parameter adjustments to minimize defects [25]. Furthermore, these modelling and data-monitoring approaches reduce reliance on costly trial-and-error, guiding informed parameter selection for process optimization [26].

In summary, DED emerges as a robust and evolving technology that bridges near-net-shape manufacturing with adaptive, precision engineering. Enhanced by integrated physics-based modelling, data-driven analytics, and real-time closed-loop monitoring, DED is rapidly advancing toward industrial maturity as a core platform for high-value, repair-centric, and functionally graded additive manufacturing [27].

2.1.1 Metal Wire Additive Manufacturing

Metal wire additive manufacturing (MWAM) is firmly rooted within the Directed Energy Deposition (DED) family and has emerged as a key enabler for large-scale, cost-efficient, and sustainable metal fabrication. By continuously feeding metal wire into a melt pool created by a laser, MWAM builds structural components layer by layer, achieving deposition rates significantly higher than powder-fed DED methods and eliminating the need for powder handling and recycling systems, this process is represented by

Figure ***1*** [28-30].

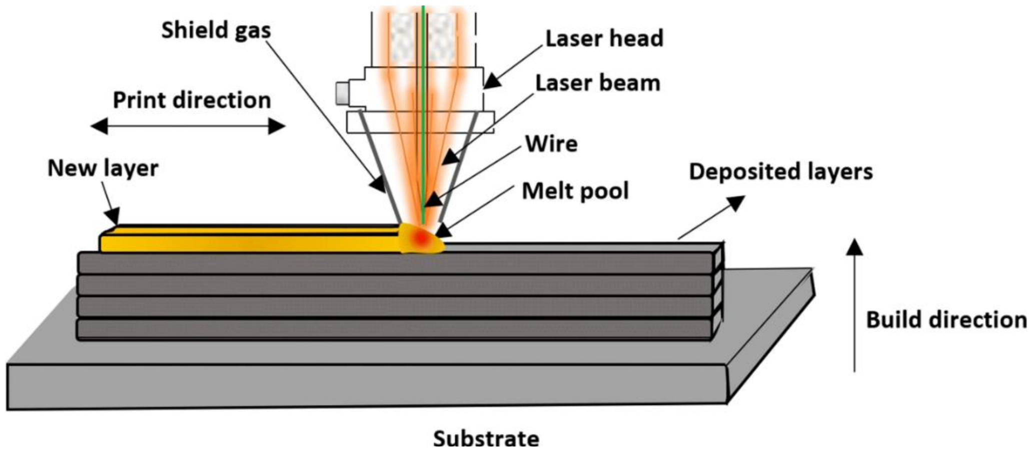

Figure 1. Schematic diagram of Wire Laser Additive Manufacturing

2.1.2 Advantages and limitations

Directed Energy Deposition (DED) is a flexible and powerful additive manufacturing (AM) technology that stands out due to its capability to fabricate, repair, and modify metal components using a concentrated energy source—such as a laser, electron beam, or arc—to melt material feedstock, typically wire or powder, Figure 2. Among its many advantages is the ability to produce large-scale parts with high deposition rates, often exceeding those of Powder Bed Fusion (PBF) processes [31,35]. This makes DED particularly attractive for sectors requiring component repair or augmentation, such as aerospace, energy, and marine industries [31,34]. Moreover, DED is compatible with a wide range of alloys, including titanium, stainless steel, Inconel, and tool steels, allowing for broad material flexibility [32].

Figure 2. Low alloy steel pipe cladded with Inconel 718

However, DED generally produces inferior surface finish and dimensional accuracy relative to processes like Powder Bed Fusion (PBF). The layer resolution in DED is typically coarser due to the larger melt pool size and wire/powder feed geometry, resulting in parts that often require extensive post-processing such as CNC machining or polishing to meet final tolerances. In contrast, PBF methods can achieve finer features and smoother surfaces due to the thin powder layers and high-precision scanning strategies [36].

The microstructure of DED-fabricated parts is often anisotropic, exhibiting direction-dependent mechanical properties due to epitaxial grain growth along thermal gradients [33,37].

Focusing more specifically on Wire Laser Additive Manufacturing (WLAM), the process involves melting a continuous metal wire using a focused laser beam to deposit material layer by layer. WLAM combines the clean energy delivery and high precision of laser systems with the material efficiency of wire feedstock [31,38]. Compared to arc-based wire deposition (e.g., WAAM), WLAM can achieve finer control over melt pool size and heat input, resulting in superior dimensional accuracy and reduced porosity [34]. Nonetheless, WLAM presents unique technical challenges, including wire-laser alignment, feed stability, and spatter formation, which can affect the consistency of deposition [38,39]. Furthermore, real-time control of the thermal gradient is essential to prevent hot cracking and to manage grain structure [35,39].

WLAM offers material efficiency approaching 100%, reduces feedstock costs by approximately 90%, and facilitates use of larger build volumes without the constraints of a sealed powder chamber—advantages that are particularly attractive for aerospace, shipbuilding, and energy applications [28-30]. LW-DED extends these benefits into high-precision domains by combining wire-feedstock with laser energy, enabling finer control over melt pool dynamics and part geometry [29].

Ongoing research is addressing these challenges through advanced path planning strategies, modelling of melt pool dynamics, and real-time feedback systems using sensors and AI-based control algorithms [37,39]. These innovations are pushing WLAM toward greater industrial maturity, enabling its use in mission-critical applications such as turbine blade repair, aerospace brackets, and tooling inserts.

2.2 Inconel 718

Inconel alloys are a family of high-performance, austenitic nickel-chromium-based superalloys widely used in extreme environments due to their excellent resistance to oxidation, corrosion, and high-temperature mechanical degradation. These alloys maintain their structural integrity at temperatures exceeding 1000 °C, making them ideal for aerospace engines, gas turbines, nuclear reactors, and petrochemical systems [40,41]. Among the most prominent members of this family is Inconel 718, a precipitation-hardenable alloy that balances high strength, creep resistance, corrosion tolerance, and weldability, enabling it to perform under both high-temperature and cryogenic conditions [42].

Inconel 718 contains significant amounts of nickel (52–55 wt.%), chromium (17–21 wt.%), iron (~18 wt.%), niobium (~5 wt.%), and smaller additions of molybdenum, titanium, and aluminium. This composition enables it to undergo precipitation strengthening, primarily via the formation of γ' ($Ni_3(Al,Ti)$) and γ'' (Ni_3Nb) phases during controlled aging. The γ''

phase is particularly important, as it provides most of the alloy's strengthening at intermediate temperatures (~650 °C), while the δ phase (orthorhombic Ni_3Nb) can also form and influence grain boundary behaviour [43,44].

When Inconel 718 is processed by Wire Laser Additive Manufacturing (WLAM), several microstructural features emerge that significantly affect the material's performance. The layer-by-layer thermal cycling inherent to DED promotes non-equilibrium solidification and often results in directionally solidified or columnar grain structures, especially in the absence of thermal management or grain refiners [45]. The rapid cooling rates and directional heat flow can suppress the formation of the desired γ′ and γ″ phases in the as-built condition, while promoting the retention of supersaturated γ matrix and the undesirable δ or Laves phases [46]. In WLAM of Inconel 718, microsegregation of niobium (Nb) is commonly observed, particularly along interdendritic regions, due to the solute rejection during solidification. This can lead to the formation of brittle Laves phase $(Ni,Fe,Cr)_2(Nb,Mo,Ti)$, which is known to degrade mechanical properties, especially ductility and fatigue life [45,47]. To mitigate this, post-processing heat treatments are crucial. A solution treatment followed by aging allows for the dissolution of Laves phase and the precipitation of strengthening γ′ and γ″ phases, Figure 3 [46,48].

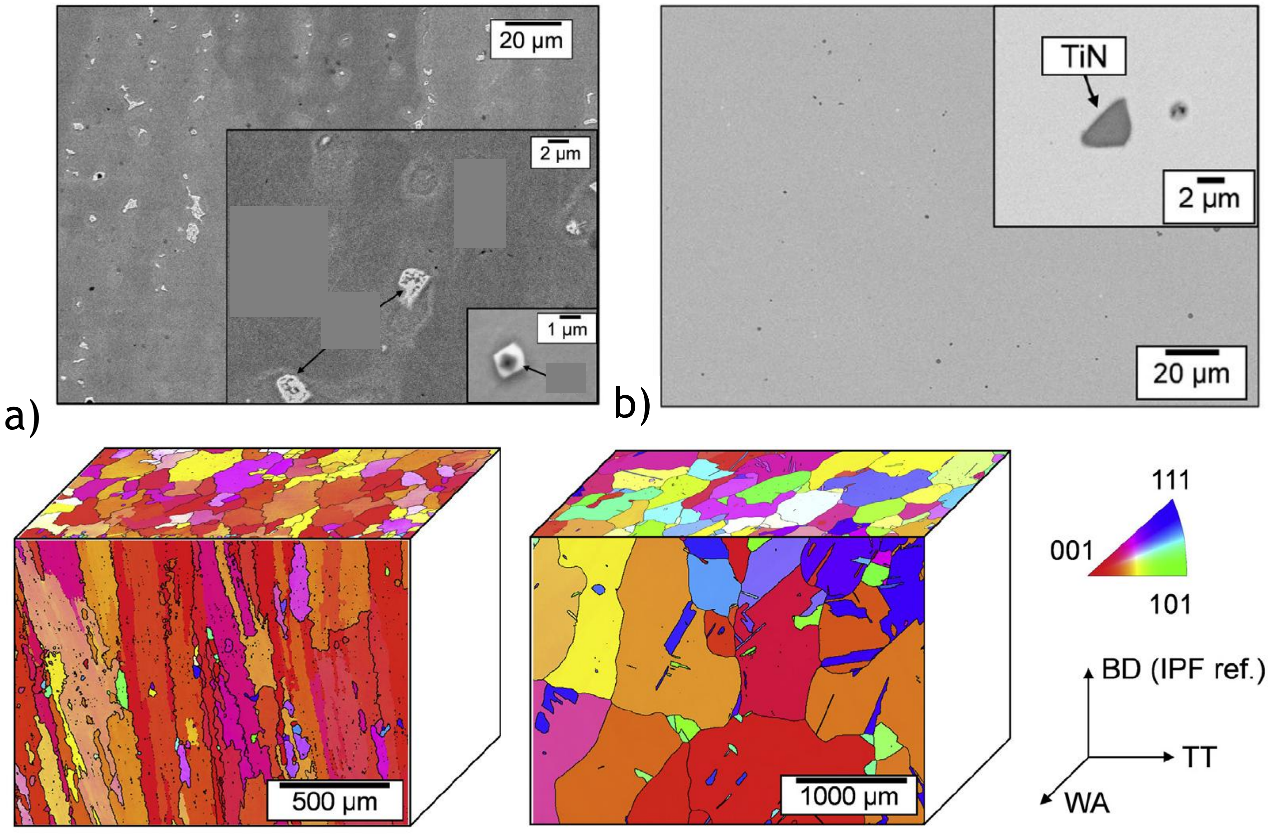

Figure 3. Inconel 718 microstructure; a) As built; b) Heat treated (adapted from [1]).

2.3 Inconel 718 Cladding on S355 and SS 304L

In DED and WLAM processes, substrates serve as the foundational base for the deposition of high-performance alloys such as Inconel 718, particularly in cladding and repair applications. The interaction between the Inconel clads and the substrate material is a key determinant of metallurgical bonding quality, dilution behaviour, residual stresses, and interface integrity [49]. During cladding, a portion of the substrate surface is locally melted to promote bonding, leading to complex thermal gradients, interdiffusion phenomena, and microstructural transitions that can either enhance or degrade the mechanical and corrosion properties of the resulting component [50,51].

Structural steels and stainless steels represent two fundamental categories of engineering materials widely used across industries due to their excellent mechanical properties, formability, weldability, and cost-effectiveness. Structural steels, such as S355, are carbon-manganese steels primarily utilized in civil engineering, construction, shipbuilding, and machinery fabrication. They offer high strength, good toughness, and ease of processing, but are generally susceptible to corrosion and oxidation, particularly in harsh or high-temperature environments [52].

Stainless steels, on the other hand, such as AISI 304L, contain significant amounts of chromium (≥10.5%) that enable the formation of a passive oxide layer, providing corrosion resistance in aqueous and mildly aggressive environments. However, stainless steels still suffer from limitations in extreme thermal conditions, under chloride attack, or in applications involving high mechanical stress, where creep, thermal fatigue, or corrosion pitting may occur [53].

To overcome these deficiencies and extend the service life of components made from structural or stainless steels, surface enhancement by cladding with nickel-based superalloys, notably 718, has gained significant traction. Inconel alloys are renowned for their exceptional oxidation resistance, thermal stability, and mechanical strength at elevated temperatures, as well as their resistance to chloride-induced stress corrosion cracking, making them ideal protective layers in severe environments [54,55].

DED-based wire laser cladding of Inconel on steel substrates creates a metallurgically bonded overlay that shields the substrate from corrosive or high-temperature degradation while retaining the structural core’s economic and mechanical benefits. This functionally graded approach allows industries to combine the best of both material classes: the strength and affordability of steels with the surface durability of superalloys [56].

The metallurgical interface is a critical point to the overall performance of the composite system. The HAZ is formed due to thermal gradients that alter the microstructure of the substrate adjacent to the fusion boundary. In the case of S355, a ferritic-pearlitic low-alloy structural steel, exposure to high thermal inputs can lead to grain coarsening, carbide precipitation, and, in some cases, the formation of brittle martensitic or bainitic phases depending on the cooling rate. This may reduce toughness and increase hardness in the HAZ, potentially initiating crack propagation under cyclic loading. In contrast, SS304L, an austenitic stainless steel with higher thermal stability and corrosion resistance, forms a more stable HAZ with less pronounced microstructural transformations, although sensitization—chromium carbide precipitation at grain boundaries—can occur under slow cooling, impacting corrosion resistance. At the fusion interface between the Inconel 718 clad and the substrate, epitaxial grain growth is commonly observed, particularly under rapid solidification conditions. This results in columnar dendrites nucleating at the substrate surface and extending into the clad. In both substrates, metallurgical bonding is generally sound, though elemental diffusion at the interface varies due to compositional differences. In the S355 interface, Fe diffusion into the Ni-rich clad can form brittle intermetallic compounds if not properly controlled. For SS304L, the interface typically exhibits a more compatible dilution profile due to the closer alloying system, leading to improved bonding and lower risk of deleterious phases. Studies have shown that optimized process parameters (laser power, travel speed, and wire feed rate) and the use of interpass temperature control can mitigate HAZ brittleness and enhance interface quality in both substrate types [57-59].

Too conclude, for structural steels like S355, cladding with Inconel 718 is especially beneficial in applications such as power plants, oil and gas infrastructure, and offshore platforms, where components are exposed to saltwater, hydrocarbons, and elevated service temperatures. Inconel layers can prevent the rapid corrosion and thermal fatigue that carbon steels alone cannot withstand [60].

In the case of stainless steels like SS304L, Inconel cladding enhances resistance to localized corrosion, wear, and oxidation, particularly in chemical processing equipment, heat exchangers, and aerospace components, where service conditions may exceed the performance thresholds of standard stainless alloys [61]. The metallurgical compatibility between SS304L and Inconel facilitates a more stable interface with fewer defects and more uniform microstructural transitions than carbon steels, thus reducing repair needs and extending component lifetimes.

2.4 Imperfections and Defects

One of the critical issues is the formation of porosity, which arises primarily due to gas entrapment within the melt pool during rapid solidification. Porosity in Inconel 718 clads can originate from several sources, including hydrogen solubility differences between the wire and substrate, inadequate shielding gas protection, or rapid solidification trapping gases within the solidified matrix [63,64]. Studies show that optimizing laser power and wire feed rate can effectively reduce porosity, but the mismatch in thermal properties between Inconel 718 and steel substrates often exacerbates this defect [65].

Cracking phenomena represent another critical defect type. Solidification cracking is often observed due to the high thermal gradients and residual stresses developed during rapid cooling, compounded by the metallurgical incompatibility at the interface between the nickel-based superalloy and the steel substrates [66]. The presence of brittle intermetallic phases at the clad-substrate interface can act as crack initiation sites, further complicating the integrity of the deposited layer. Cold cracking induced by hydrogen diffusion into the heat-affected zone is also reported, especially in the S355 steel substrate, which is more susceptible to hydrogen embrittlement [67]. Preheating of the substrate and controlling heat input during deposition have proven effective in mitigating these cracks [68].

Surface quality issues such as roughness and irregular morphology are frequently reported in WLAM. These defects are influenced by the interaction of process parameters with the distinct thermal conductivities and melting points of the substrates. The stair-stepping effect and partial melting at layer boundaries can lead to uneven layer thickness and poor adhesion, impacting the final dimensional accuracy and requiring extensive post-processing [69,70].

Microstructural heterogeneity in the deposited Inconel 718 layers, including coarse dendritic structures and segregation of alloying elements such as Nb and Ti, is another source of concern. These inhomogeneities can weaken the mechanical properties and reduce corrosion resistance [71]. Moreover, the formation of deleterious phases such as Laves and delta phase in the interfacial region between Inconel 718 and the steel substrate can cause embrittlement and degrade performance [72]. Recent advances in *in-situ* thermal monitoring and adaptive process control have demonstrated promise in stabilizing microstructure during WLAM deposition, improving the quality of the clads [73].

Another critical defect observed is the lack of sufficient melting area and poor adhesion at the clad-substrate interface. This phenomenon is often linked to inadequate wettability of the molten Inconel 718 on the steel surfaces, resulting in incomplete fusion and weak metallurgical bonding. Wettability is influenced by the surface energy differences between the nickel-based alloy melt and the steel substrate, as well as by the presence of oxide layers or contaminants on the substrate surface, which can act as barriers to effective bonding. Insufficient laser energy input or inappropriate scanning strategies can lead to a reduced melt pool size, limiting the interaction area between the deposited material and the substrate and causing incomplete melting and fusion. This poor adhesion manifests as interfacial gaps or lack of fusion defects, which degrade load transfer efficiency and can serve as crack initiation sites during service. Improving substrate surface preparation, such as mechanical cleaning or chemical etching, combined with optimized laser parameters to ensure adequate energy density and melt pool dynamics, has been shown to enhance wettability and adhesion, thereby minimizing these interface defects [74].

3. Methodology

3.1 Preparation of Test Pieces

To evaluate the quality of the Inconel 718 clads produced by DED Laser Multi Wire - PAMPROD, Figure 4, 5 plates of S355 and 1 plate of 304L containing between 9 and 10 clads were divided to isolate each clad and cut in half to produce two samples from each clad. The plate with the clads and cuts made can be seen in Figure 5. The cut was made using a band saw. The chemical composition of the Inconel clad, 304L plate and S355 plates can is showed in

Table 1, Table 2, and Table 3 respectively.

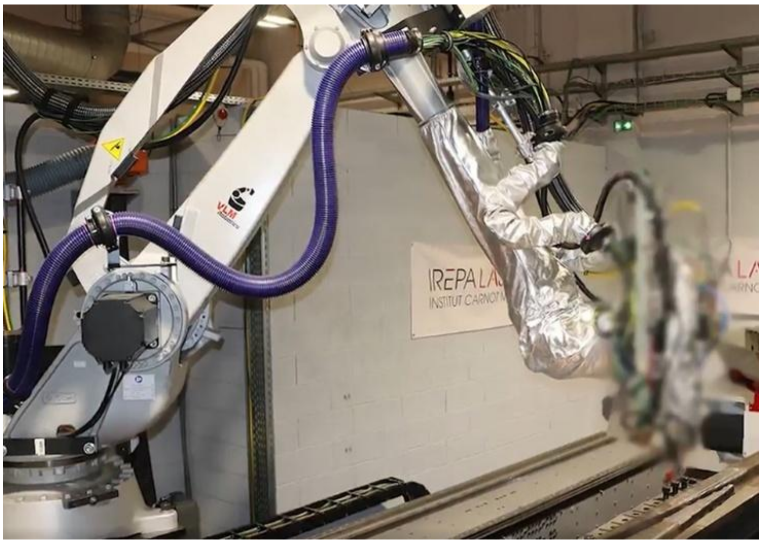

Figure 4. DED Laser Multi Wire – PAMPROD.

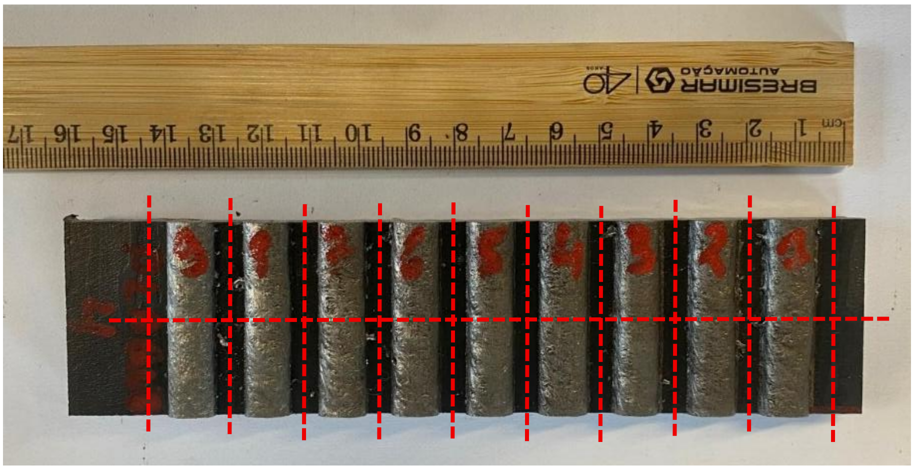

Figure 5. S355 Plate 4.

Table 1. Inconel 718 chemical composition (wt.%).

Inconel 718 clad material	**C**	**Ni**	**Cr**	**Fe**	**Nb**	**Mo**	**Ti**	**Cu**
	0.08 max	50-55	17-21	balance	4.75-5.50	2.80-3.30	0.65-1.15	0.30 max
	Al	**Co**	**Mg**	**Si**	**P**	**S**	**B**	
	0.20-0.80	1 max	0.35 max	0.35 max	0.015 max	0.015 max	0.06 max	

Table 2. 304L plate chemical composition (wt.%).

304L plate	**C**	**Cr**	**Ni**	Mg	**S**	**N**	**P**	**S**
	0.03 max	17.50-19.50	8-12	2 max	0.75 max	0.10 max	0.045 max	0.030 max

Table 3. S355 plates chemical composition (wt.%).

S355 plates	**C**	**Mn**	**Si**	**P**	**S**	**Cu**	**N**
	0.24 max	1.60 max	0.55 max	0.040 max	0.040 max	0.040 max	0.012 max

The samples were named acording to the substrate material, processing parameters: laser power, laser speed, wire deposition speed, argon speed, scanning speed not represented as it is common for all samples (0.54 m/min) and plate and clad number. An example would be for the first sample: SS [8.5 0.5 4 4] (plate 1, clad 1), and for the last sample: S [9.6 0.6 4.9 4] (plate 6, clad 5). These parameters can be seen in Table 4. and Table 5.

Table 4. Inconel 718 deposited on stainless steel 304L samples production parameters.

		Name			
Plate	**Clad**	**Laser power (KW)**	**Laser speed (m/min)**	**Wire deposition speed (m/min)**	**Argon pressure (bar)**
1	**1**	8.5	0.5	4	4
	2	8.5	0.5	4	4
	3	8.5	0.75	4	4
	4	9	0.5	5	4
	5	9	0.75	5	4
	6	9	0.75	5	2
	7	9	0.75	5	2
	8	8.5	0.55	5	2

	9	8.5	0.55	5	2
	10	8.5	0.7	5	3

Table 5. Inconel 718 deposited on structural steel S355 samples production parameters.

		Name			
Plate	**Clad**	**Laser power (KW)**	**Laser speed (m/min)**	**Wire deposition speed (m/min)**	**Argon pressure (bar)**
2	**1**	7.5	0.7	5	3
	2	8	0.55	5	3
	3	9	0.55	5	3
	4	9.5	0.7	5	3
	5	9	0.75	5	3
	6	9	0.75	5	3
	7	9	0.75	5	3
	8	9.5	0.75	5	3
	9	9.5	0.75	4.75	3
3	**1**	9	0.65	5	4
	2	9	0.65	5	4
	3	9	0.65	5	4
	4	9	0.5	5	4
	5	8.5	0.5	4.75	4
	6	8.75	0.55	4.75	4
	7	9.25	0.55	4.75	4
	8	9.25	0.55	4.75	4
	9	9.25	0.55	4.75	4
4	**1**	9.5	0.55	4.75	4
	2	9.5	0.65	4.75	4
	3	9.5	0.75	4.75	4
	4	9.5	0.55	4.5	4
	5	8.5	0.55	4.5	4
	6	9	0.55	4.5	4
	7	9	0.55	4.5	4
	8	8.5	0.55	4.5	4
	9	8.75	0.55	4.5	4

Table 5. Inconel 718 deposited on structural steel S355 samples production parameters (continuation).

		Name			
Plate	**Clad**	**Laser power (KW)**	**Laser speed (m/min)**	**Wire deposition speed (m/min)**	**Argon pressure (bar)**
5	**1**	8.75	0.55	4.5	4
	2	8.75	0.55	4.5	4
	3	8.75	0.55	4.5	4
	4	9	0.55	4.5	4
	5	9	0.6	4.75	4
	6	9.5	0.6	4.75	4
	7	9.5	0.6	4.75	4
	8	9.5	0.6	4.75	4
	9	9.6	0.6	4.75	4
6	**1**	9.6	0.6	4.9	4
	2	9.6	0.6	5	4
	3	9.6	0.6	5	4
	4	9.6	0.6	5	4
	5	9.6	0.6	4.9	4

3.2 Digital Microscopy Examination

To better understand the overall quality of the clads and presence of the defects, all samples were subjected to a digital microscopy analysis. In this analysis the width, heigh and area the clad, depth, area of the melted zone and contact angles have been measured as seen in Figure 6. These measurements are essential to characterize the samples and provide a lot of information about their overall appearance. The dilution, which is another essential parameter of a clad, because it directly correlates to how well the clad and substrate mix together to provide a stronger bonding, was calculated using Equation 1. Furthermore, all defects present in each sample were identified and grouped as one of the following possible defects: cracks (c), large porosities (lp), and small porosities (sp). The location of the cracks and large porosities was also noted as being in the upper (u), middle (m) or lower (l) parts of the clads as seen in Figure 7 [75].

For this examination, metallographic preparation was performed. The specimens were ground and polished with silicon carbide sandpapers, followed by polishing with 6 and 1 µm diamond suspension on the appropriate cloths.

$$Dilution\ \% = \frac{Clad\ Area}{Clad\ Area + Melted\ Area} \times 100$$ **Equation 1**

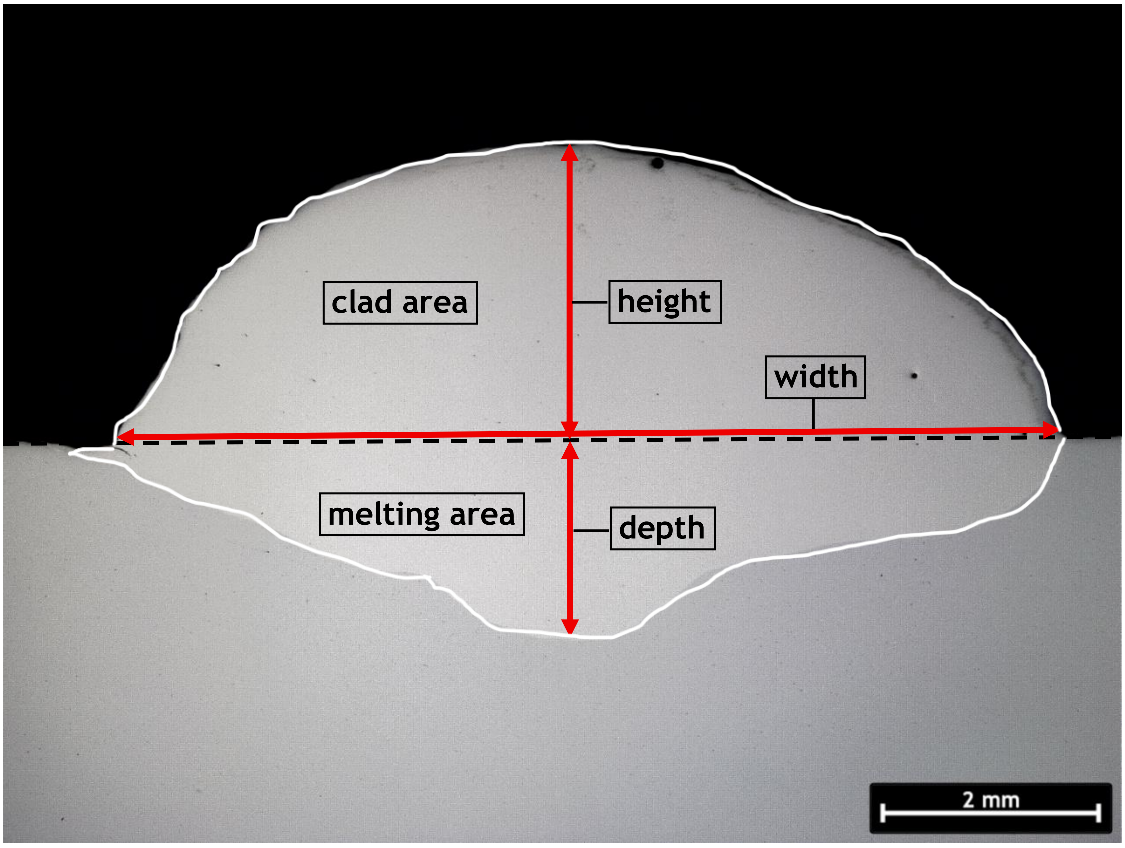

Figure 6. Clad measurements.

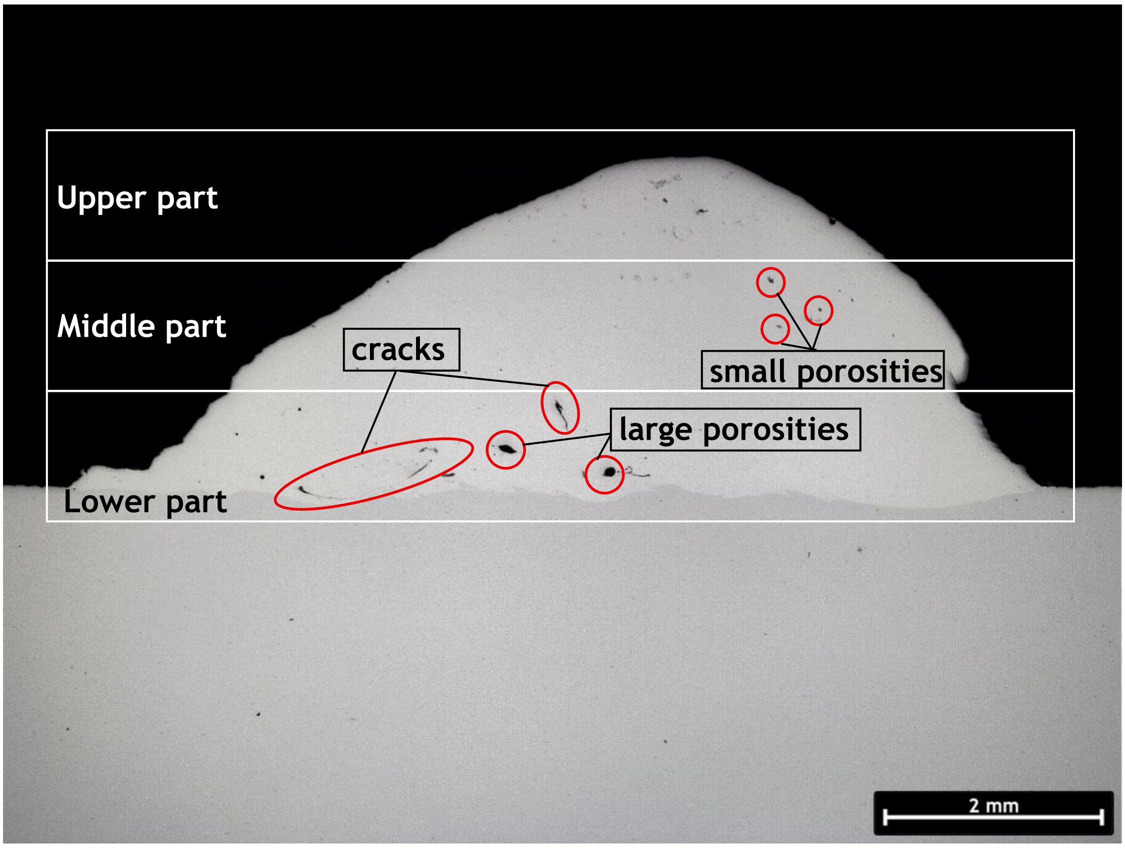

Figure 7. Clad defects.

3.3 Heat Treatments

Post-deposition heat treatments are essential for improving the microstructure and mechanical properties of Inconel 718 fabricated via Wire Laser Additive Manufacturing (WAAM), which typically exhibits coarse columnar grains and segregation-induced Laves phase in the as-deposited condition. Seow et al. investigated multiple heat treatment strategies, focusing particularly on the mitigation of Laves phase and the development of isotropic mechanical properties. The conventional heat treatment, termed Standard HSA, involved a homogenisation at 1100 °C for 1 hour followed by solution treatment at 980 °C for 1 hour, air cooling after each step, and a subsequent double aging cycle (720 °C for 8 h furnace cooled, then 620 °C for 8 h air cooled). Although this route successfully dissolved Laves phase, it also resulted in undesirable δ-phase precipitation at grain boundaries, known to embrittle the material. To address this, a modified HA treatment was developed, comprising a single-step homogenisation at 1186 °C for 40 minutes—just above the eutectic temperature of Laves phase—followed directly by the same double aging schedule. This modified regime successfully dissolved Laves phase without δ-phase formation, while also reducing grain texture intensity and anisotropy in mechanical properties [1].

Based on this study, a similar heat treatment cycle was performed, although with a small variation, as seen in Figure 8. The solubilization temperature was higher than the modified heat treatment of the study, due to the lower precision of temperature control of the muffle furnace used, in order to ensure the temperature was always above the dissolution temperature of the Laves phase, 1185 °C. For that reason, the temperature 1200 ºC was applied for 45 minutes for the homogenization treatment and subsequent double aging cycle, 720 °C for 8 h furnace cooled, then 620 °C for 8 h air cooled, of block from where the tensile specimens were later obtained. For preliminary studies samples S [9.6 0.6 4.75 4] (plate 5, clad 9) and S [9.6 0.6 4.9 4] (plate 6, clad 5) were submitted shorter homogenisation times, 15 and 10 minutes respectively, due to having very small dimensions. The double aging performed followed the standard, 720 °C for 8 h furnace cooled, then 620 °C for 8 h air cooled.

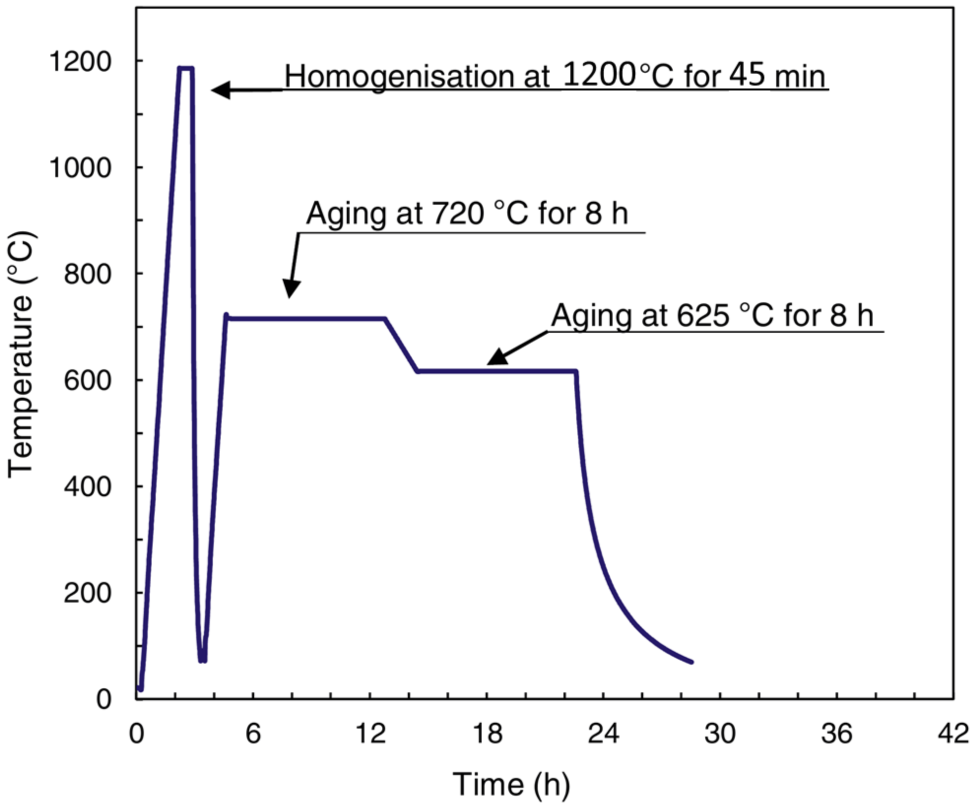

Figure 8. Heat treatment cycle.

3.4 Scanning Electron Microscopy

Scanning Electron Microscopy Spectroscopy (SEM) was performed to analyse the microstructure of the clad, interface and substrate materials. SEM EDS was used to identify the chemical composition of the clad and substrate materials, observed inclusions and laves phase. Electron backscatter diffraction (EBSD) analysis has been used to assist with phase identification, grain size and orientation. The data obtained from EBSD were submitted to a dilation clean-up procedure, using a grain tolerance angle of 15° and the minimum grain size of 10 points, to avoid inaccurate predictions. These analyses were done with a FEI QUANTA 400 FEG (FEI Company, Hillsboro, OR, USA) with and energy-dispersive detector (EDS) and energy dispersive spectroscopy (EBSD).~

3.5 Hardness Test

Vickers low force hardness tests with a load of 0.3 KgF with a dwell time of 15 seconds were performed. The indentations were made in a profile setting with a 1 mm step, in order to understand the hardness variation from the whole of the clad, interface and substrate material. The hardness values were obtained with a Innova Test, Falcon 400 Vickers hardness.

3.6 Tensile Test

Tensile tests were performed to perform a mechanical characterization of specimens obtained from a deposited Inconel 718 block with and without heat treatments. The specimens were taken both horizontal, vertical and diagonal directions. The tests were performed with a Instron 5900 using a 100KN load cell, with a speed rate of 1 mm/s. The measurements were made via image correlation with the software VIC 2D. The dimensions of the specimens are specified in Figure 9.

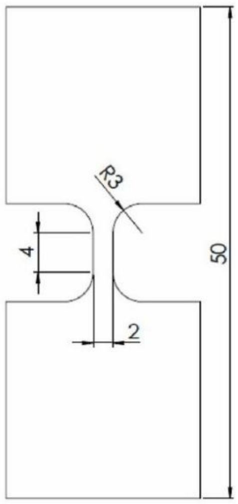

Figure 9. Tensile specimen.

4. Results and Discussion

4.1 Digital Microscopy Analysis

After an extensive analysis of the samples, Table 6 and Table 7, was constructed containing for each clad the following information: width (mm), height (mm), depth (mm), clad area (mm^2), melt area (mm^2), dilution %, contact angle (°) and defects. To understand which processing parameters achieved the best results and thus select samples for further analysis, a number of criteria were applied. These criteria were: a clad area >25 mm^2, guarantying that there is a high deposition rate of material for the clads. A dilution (%) > 14.5%, in order to guarantee a strong bonding between the clad and the substrate. An average contact angle <90º, while not having any angle >100º, ensuring a good wettability. Finally, all the defects were noted, and only small porosities, <150 micron, would be acceptable, meaning, any cracks or large porosities would exclude that clad.

The analysis resulted in seven samples fulfilling all the criteria, three of 304L stainless substrate clads: SS [8.5 0.5 4 4] (plate 1, clad 1), SS [8.5 0.55 5 2] (plate 1, clad 8), SS [8.5 0.55 5 2] (plate 1, clad 9), and four of S355 structural steel substrate clads: S [8.75 0.55 4.5] (plate 5, clad 1), S [8.75 0.55 4.5 4] (plate 5, clad 2), S [9.6 0.6 4.75 4] (plate 5, clad 9) and S [9.6 0.6 4.9 4] (plate 6, clad 5). These samples can be seen in Figure 10.

From the data gathered, the best results of the clads deposited in the 304L Stainless Steel were the clads produced using a 8.5 KW laser power, 0.5 m/min laser speed, 4 m/min wire feed rate and 4 bar argon (SS [8.5 0.5 4 4] (plate 1, clad 1)), and the two clads produced using a 8.5 KW laser power, 0.55 m/min laser speed, 5 m/min wire feed rate and 2 bar argon (SS [8.5 0.55 5 2] (plate 1, clad 8) and SS [8.5 0.55 5 2] (plate 1, clad 9)). This suggests that, to produce clads on a 304L stainless steel, a laser power of 8.5 KW seems to be the most optimal, this laser power was the same used in every clad that met the criteria, while all clads using a higher power, 9KW failed to fulfil the criteria. The laser speed of 0.5 and 0.55 m/min both produced clads without major defects. All clads produced with a laser speed above 0.55 m/min presented defects, meaning that an interval between 0.5 and 0.55 m/min laser speed can produce good clads. A wire feed rate between 4 and 5 m/min both produce good results, other speeds were not tested for the stainless steel subtract clads. The argon pressure was tested at 2, 3 and 4 bar, good results were obtained with both 2 and 4 bar but not at 3 bar. Although, it is more likely that an interval between 2 and 4 bar works, and the defects present in the sample SS [8.5 0.7 5 3] (plate 1, clad 10) are due to the higher laser speed used, 0.7 m/min and not caused by the argon pressure. Despite sample SS [8.5 0.5 4 4] (plate 1, clad 1) not presenting any major defects and fulfilling the rest of the criteria, sample SS [8.5 0.5 4 4] (plate 1, clad 2), produced with the same parameters did not fulfil the wettability or the lack major defects criteria. On the other hand, samples SS [8.5 0.55 5 2] (plate 1, clad 8) and SS [8.5 0.55 5 2] (plate 1, clad 9), both produced with the same parameters, fulfil all criteria. This leads to conclude that the parameters used to produce sample SS [8.5 0.5 4 4] (plate 1, clad 1) as defect free, are not always replicable, while for the parameters used to produce (SS [8.5

0.55 5 2] (plate 1, clad 8) and SS [8.5 0.55 5 2] (plate 1, clad 9) seem to result more consistently in samples that fulfil all criteria.

For the reasons presented previously it is recommended that in order to produce Inconel clads on a 304L stainless steel, the parameters used are: 8.5 KW laser power, 0.55 m/min laser speed, 5 m/min wire feed rate and 2 bar argon.

Moving to the clads deposited in the structural steel S355, the best results were achieved using an 8.75 KW laser power, 0.55 m/min laser speed, 4.5 m/min wire feed rate and 4 bar argon (S [8.75 0.55 4.5 4] (plate 5, clad 1) and S [8.75 0.55 4.5 4] (plate 5, clad 2). With a 9.6 KW laser power, 0.6 m/min laser speed, 4.75 m/min wire feed rate and 4 bar argon (S [9.6 0.6 4.75 4] (plate 5, clad 9)). And also using a 9.6 KW laser power, 0.6 m/min laser speed, 4.9 m/min wire feed rate and 4 bar argon (S [9.6 0.6 4.9 4] (plate 6, clad 5). Opposite to what happened in the clads deposited on stainless steel, in which laser power above 8.5KW lead to defects, for the S355 substrate, both a laser power of 8.75KW and 9.6KW produced clads fulfilling criteria. For the laser speed, both 0.55 and 0.6 m/min laser speeds resulted in good clads, the higher laser speed (0.6 m/min) was used for the higher laser powder (9.6KW). In terms of wire feed rate, 4.5, 4.75 and 4.9 m/min produced good results, being 4.5 m/min rate used for the 8.5KW, while a higher laser power was matched with higher wire feed rates, 4.75 and 4.9 m/min. An argon pressure of 4 bar was common to all good clads, only for plate 2, a different argon pressure was tested, 3 bar, and any clad met the criteria. An overall analysis shows that besides S [8.75 0.55 4.5 4] (plate 5, clad 1) and S [8.75 0.55 4.5 4] (plate 5, clad 2), two other clads produced with an 8.75 KW laser power, 0.55 m/min laser speed, 4.5 m/min wire feed rate and 4 bar argon, S [8.75 0.55 4.5 4] (plate 4, clad 9) and S [8.75 0.55 4.5 4] (plate 5, clad 3) did not met the criteria, meaning these parameters led to 50% acceptable clads. For a 9.6 KW laser power, 0.6 m/min laser speed, 4.9 m/min wire feed rate and 4 bar argon, used in S [9.6 0.6 4.9 4] (plate 6, clad 5), there was another clad produced with these properties that did not met the criteria, S [9.6 0.6 4.9 4] (plate 6, clad 1), resulting also in a 50% rate of fulfilling all the criteria with these parameters. Only with a 9.6 KW laser power, 0.6 m/min laser speed, 4.75 m/min wire feed rate and 4 bar argon S [9.6 0.6 4.75 4] (plate 5, clad 9), resulted in 100% rate of achieving all criteria. This might indicate that a slightly lower wire feed rate of 4.75 m/min instead of 4.9 m/min might be optimal. However, only one clad was produced with these parameters and it is necessary to produce more to understand if all clads would continue to meet the criteria.

For the reasons exhibited previously it is recommended that in order to produce Inconel 718 clads on a S355 structural steel, the parameters used are: 9.6 KW laser power, 0.6 m/min laser speed, 4.9 m/min wire feed rate and 4 bar argon.

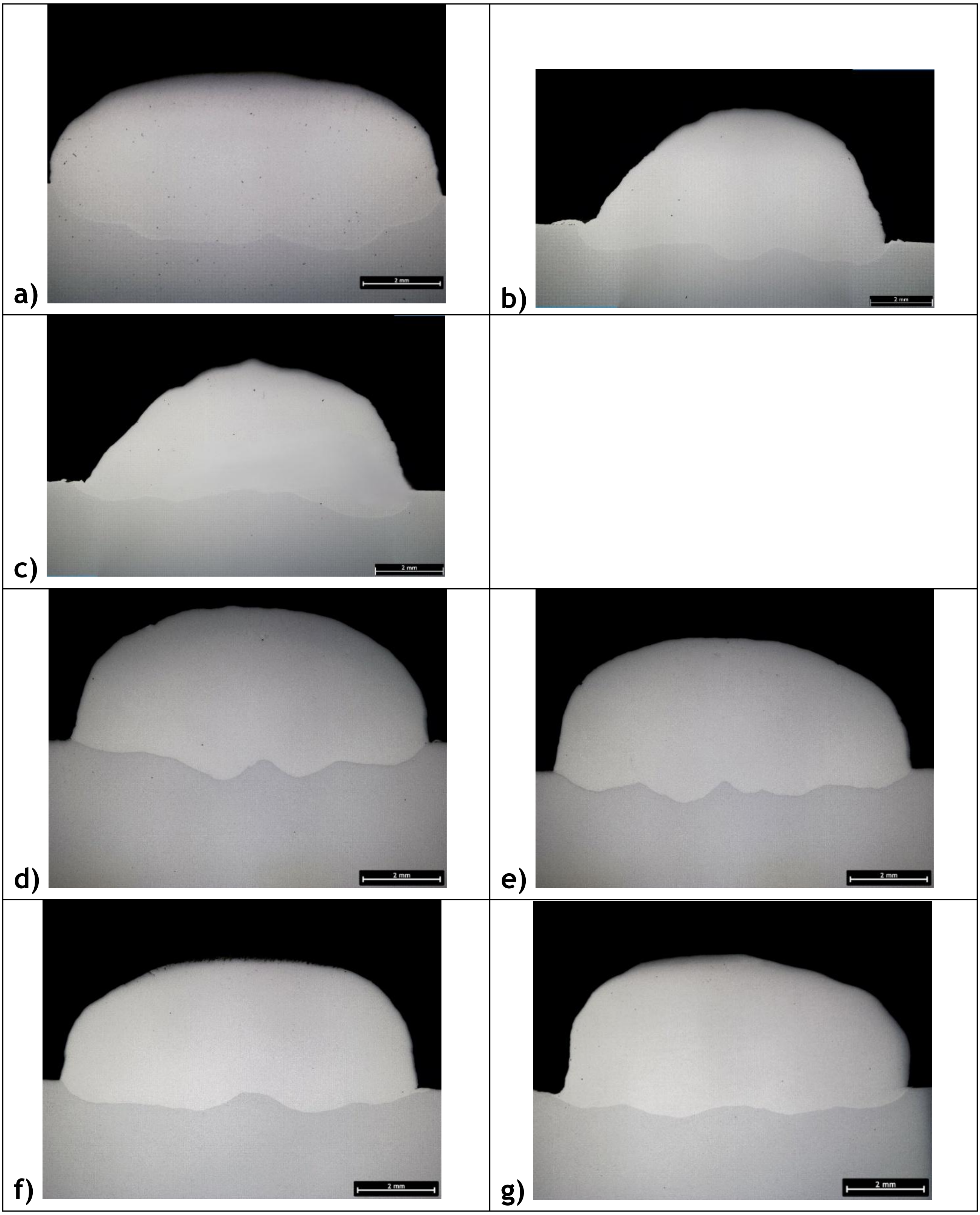

Figure 10. Digital microscopy samples; a) SS [8.5 0.5 4 4] (plate 1, clad 1); b) SS [8.5 0.55 5 2] (plate 1, clad 8); c) SS [8.5 0.55 5 2] (plate 1, clad 9); d) S [8.75 0.55 4.5 4] (plate 5, clad 1); e) S [8.75 0.55 4.5 4] (plate 5, clad 2); f) S [9.6 0.6 4.75].

Table 6. Inconel 718 deposited on stainless steel 304L samples measurements.

Measurements										Selections
Plate	Clad	Width (mm)	Height (mm)	Depth (mm)	Clad Area (mm^2)	Melt Area (mm^2)	Dilution %	Contact Angle (°)	Defects	
1	1	10.20	3.05	1.51	25.60	11.38	30.8%	96/73.9	sp	x
	2	9.91	3.17	1.35	26.108	8.87	25.4%	105.5/71.4	c(l)/lp(l)/sp	
	3	8.92	2.71	0.96	17.57	5.17	22.7%	62.9/ 87.6	lp(u)/sp	
	4	9.98	3.66	1.10	32.05	7.01	17.9%	101.6/101.3	lp(u)/sp	
	5	8.47	3.30	0.69	22.59	3.86	14.6%	92/75.8	sp	
	6	8.77	3.56	1.01	22.36	5.58	20.0%	55.7/69.2	sp	
	7	8.54	2.97	1.54	14.86	8.17	35.5%	36.9/55.9	sp	
	8	9.74	4.07	0.85	28.41	6.51	18.6%	63.2/70.5	sp	x
	9	9.49	3.78	0.84	25.68	4.42	14.7%	52.8/70.3	sp	x
	10	8.98	3.60	0.80	23.85	4.41	15.6%	59.2/73.3	sp	

Table 7. Inconel 718 deposited on structural steel S355 samples measurements.

Measurements										Selections
Plate	Clad	Width (mm)	Height (mm)	Depth (mm)	Clad Area (mm^2)	Melt Area (mm^2)	Dilution %	Contact Angle (°)	Defects	
2	1	9.05	3.07	0.21	16.53	0.79	4.6%	44.2/56.2	c(l)/lp(l)/sp	
	2	9.26	4.03	0.48	26.63	1.78	6.3%	61.8/69.8	c(l)/lp(u,l)/sp	
	3	8.64	4.39	0.73	28.55	4.08	12.5%	63.9/77.6	lp(u)/sp)	
	4	8.31	3.76	0.65	20.90	4.28	17.0%	61.1/61	lp(u)/sp	
	5	8.90	3.48	0.44	20.29	2.33	10.3%	58.7/54.4	sp	
	6	9.69	2.83	0.37	18.81	1.64	8.0%	42.3/40.5	lp(u)/sp	
	7	9.89	3.27	0.34	21.53	1.25	5.5%	56.9/40.8	c(l)/lp(u)/sp	
	8	9.90	3.03	0.43	20.02	2.74	12.0%	52.8/48.6	sp	
	9	9.84	3.17	0.55	20.88	3.57	14.6%	58.4/48.35	sp	
3	1	9.84	3.97	0.66	24.97	3.51	12.3%	45.7/74.3	c(l)/sp	
	2	9.11	3.93	0.88	25.31	4.75	15.8%	67.0/73.1	c(l)/sp	
	3	8.57	3.84	0.70	23.76	4.01	14.4%	85.9/69.9	c(l)/sp	
	4	9.96	3.65	0.68	27.61	3.17	10.3%	78.5/101.5	lp(u)/sp	
	5	10.41	3.84	0.57	30.26	2.99	9.0%	67.9/85.4	lp(l)/sp	
	6	10.36	3.12	0.58	24.08	2.27	8.6%	68.5/59.7	sp	
	7	10.60	3.11	0.49	25.20	2.04	7.5%	76.5/68.5	sp	
	8	10.16	3.28	0.47	26.58	1.97	6.9%	73.0/87.7	sp	
	9	10.22	3.15	0.56	23.80	1.79	7.0%	91.2/87.1	lp(l)/sp	

Table 7. Inconel 718 deposited on structural steel S355 samples measurements (continuation).

Measurements										Selections
Plate	**Clad**	**Width (mm)**	**Height (mm)**	**Depth (mm)**	**Clad Area (mm^2)**	**Melt Area (mm^2)**	**Dilution %**	**Contact Angle (°)**	**Defects**	
4	1	9.82	3.41	0.43	26.64	2.51	8.6%	70.3/77.7	sp	
	2	9.56	3.08	0.56	23.07	2.82	10.9%	68.7/70.1	sp	
	3	9.14	2.93	0.41	20.34	1.68	7.6%	72.3/67.9	sp	
	4	9.96	3.34	0.64	26.46	3.95	13.0%	77.8/76.1	lp(u)/sp	
	5	9.78	3.38	0.26	25.83	0.92	3.4%	75.8/75.6	sp	
	6	9.39	3.28	0.77	24.42	3.82	13.5%	79.9/73.9	sp	
	7	9.58	3.43	0.74	25.03	4.30	14.7%	76.2/72.2	lp(l)/sp	
	8	9.76	3.50	1.10	28.10	6.49	18.8%	79.2/82.5	lp(u)/sp	
	9	9.77	3.27	0.55	26.09	2.63	9.1%	78.0/79.3	lp(u)/sp	
5	1	9.38	3.54	1.02	26.16	5.05	16.2%	75.8/84.8	sp	x
	2	9.28	3.44	0.83	26.01	4.61	15.1%	79.4/82.6	sp	x
	3	10.24	3.39	0.15	24.68	0.18	0.7%	66.5/73.0	c(l)/lp(l)/sp	
	4	9.29	3.52	0.36	27.14	2.13	7.3%	87.2/85.0	sp	
	5	10.91	3.50	0.25	27.60	0.07	0.2%	134.5/79.7	c(l)/lp(l)/sp	
	6	9.71	3.35	0.84	26.41	4.15	13.6%	82.9/76.3	sp	
	7	9.65	3.35	0.70	26.34	3.73	12.4%	80.3/71.3	lp(u)/sp	
	8	9.05	3.14	0.64	23.31	3.62	13.4%	79.4/97.9	lp(u)/sp	
	9	9.34	3.34	0.71	25.75	4.68	15.4%	79.4/80.6	sp	x
6	1	8.86	3.57	0.79	26.72	5.20	16.3%	98.1/101.3	lp(u)/sp	
	2	8.88	2.75	1.89	17.42	9.83	36.1%	56.4/70.9	c(l)/lp(u)/sp	
	3	8.15	2.93	1.76	17.66	7.76	30.5%	70.9/77.3	sp	
	4	8.88	3.76	0.94	27.48	5.09	15.6%	83.1/101.0	lp(l)/sp	
	5	9.03	3.48	0.75	25.76	4.78	15.7%	78.5/94.1	sp	x

4.2 SEM/EDS and EBSD Analysis

Seven samples, three stainless steel samples, SS [8.5 0.5 4 4] (plate 1, clad 1), Figure 11, SS [8.5 0.55 5 2] (plate 1, clad 8), Figure 12, SS [8.5 0.55 5 2] (plate 1, clad 9), Figure 13, and four of S355 structural steel substrate clads: S [8.75 0.55 4.5] (plate 5, clad 1) Figure 14, S [9.6 0.6 4.75 4] (plate 5, clad 9), Figure 15, S [9.6 0.6 4.9 4] (plate 6, clad 5) Figure 16, and S [9.6 0.6 4.9 4] (plate 6, clad 5) heat treated Figure 17, were analysed with SEM, SEM/EDS and EBSD to perform a microstructural characterization.

The EBSD and SEM analyses revealed that the grain morphology throughout the as built clads is predominantly columnar, covering several millimetres in length. These columnar grains are oriented parallel to the build direction, extending from the substrate, clad interface toward the top surface of the deposited layer. Near the interface, grains appear more elongated and thinner, indicative of a high thermal gradient and directional solidification conditions imposed by the rapid heat extraction into the relatively cooler steel substrate. As solidification progresses upward, the grain width increases significantly. This grain coarsening toward the top of the clad is consistent with a reduction in the thermal gradient and slower cooling rates near the free surface.

Such microstructural evolution is typical of Inconel 718 fabricated via WLAM, where the solidification front follows the isotherms shaped by the heat source and substrate geometry. According to Seow et al. the formation of large columnar grains is driven by epitaxial growth from the substrate or previous layers, a mechanism favoured by the relatively low nucleation undercooling associated with the high thermal conductivity of steel substrates. Additionally, the competitive growth of grains aligned with the maximum thermal gradient results in the suppression of equiaxed grains, further promoting a columnar structure.

To further assess crystallographic orientation and texture development, Inverse Pole Figure (IPF) maps were generated from the EBSD scans for each of the six cladding samples. Despite the clear presence of columnar grains observed in the microstructure, the IPF maps do not reveal a strong preferential crystallographic orientation along the build direction. In other words, no dominant texture component was detected across the clads, and the orientation of grains appeared relatively random within the columnar structure.

This absence of strong crystallographic texture may be attributed to multiple factors. First, in wire laser additive manufacturing of Inconel 718, the direction of solidification tends to follow the heat flow path, which is generally upward and slightly outward from the substrate. However, due to layer-wise thermal cycling and localized remelting, epitaxial grain growth can be interrupted or redirected between successive layers, leading to misaligned grain orientations across the height of the clad.

Moving to the analysis of sample S [9.6 0.6 4.9 4] (plate 6, clad 5) heat treated, after solution treatment and aging, the once prominent columnar grains became notably smaller and more equiaxed. This grain evolution enhances isotropy, reduces texture intensity, and often leads to superior toughness and fatigue resistance in Inconel 718 components.

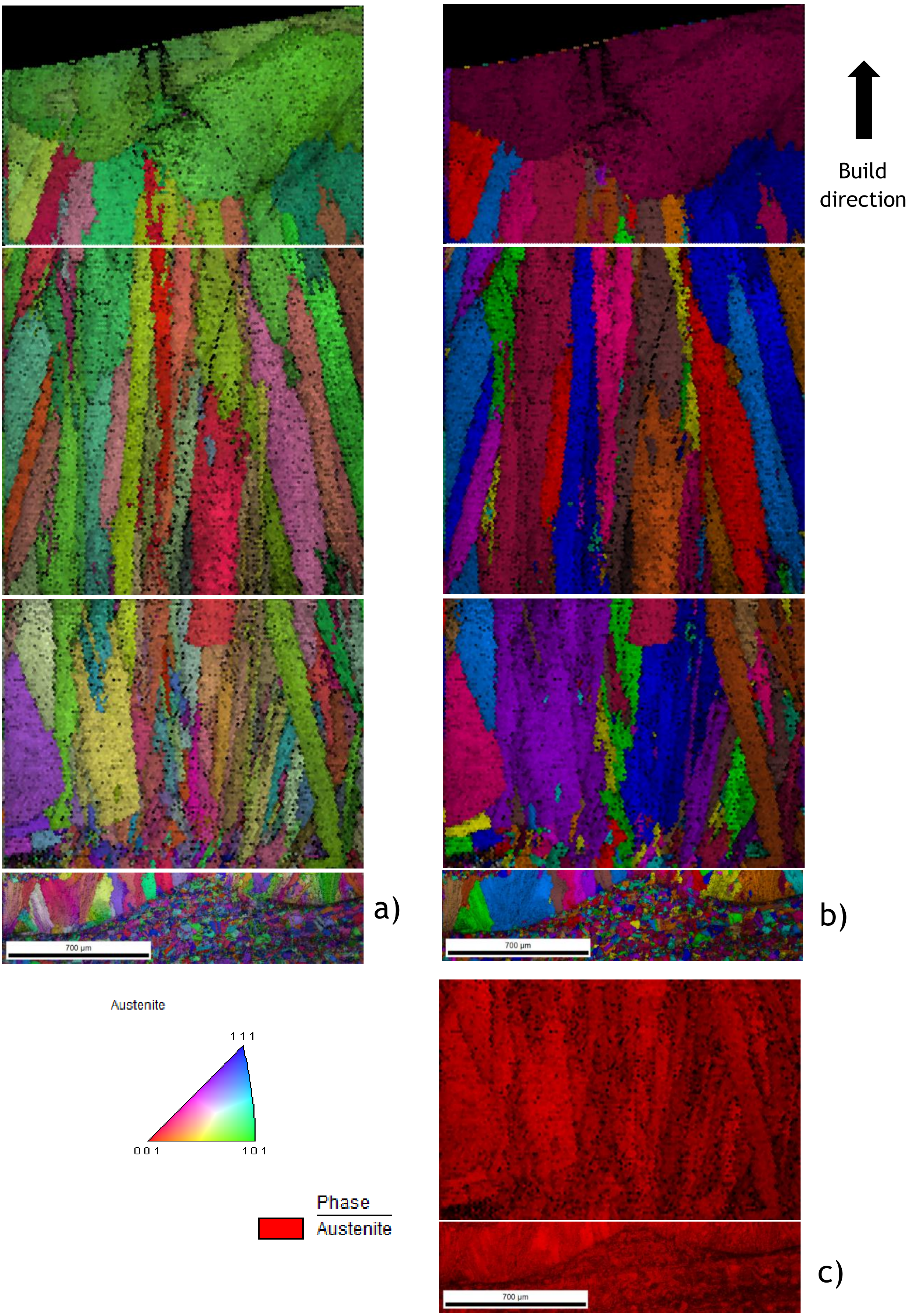

Figure 11. Inverse pole figure map a); grain map b); phase map c); of sample SS [8.5 0.5 4 4] (plate 1, clad 1).

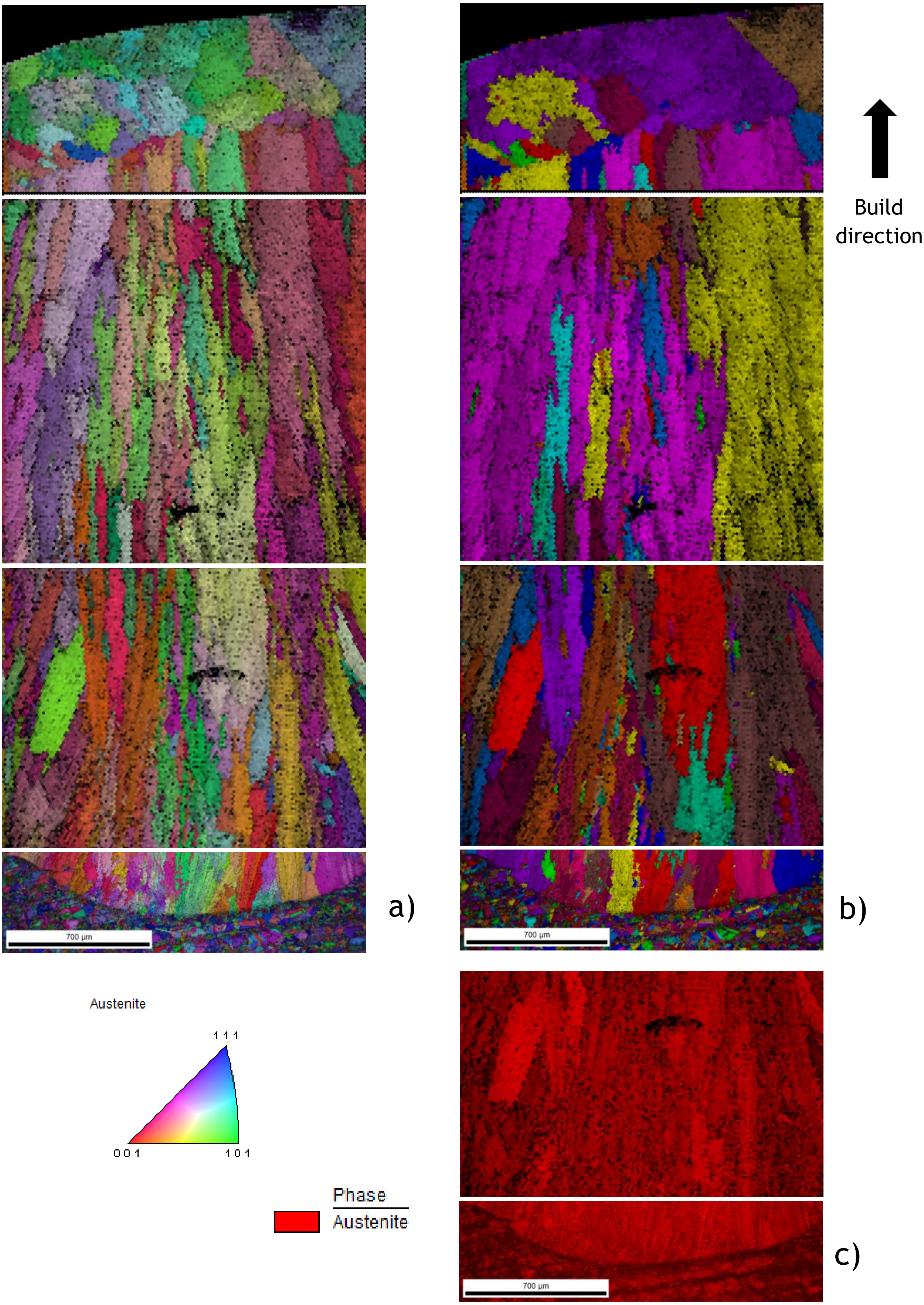

Figure 12. Inverse pole figure map a); grain map b); phase map c); of sample SS [8.5 0.55 5 2] (plate 1, clad 8).

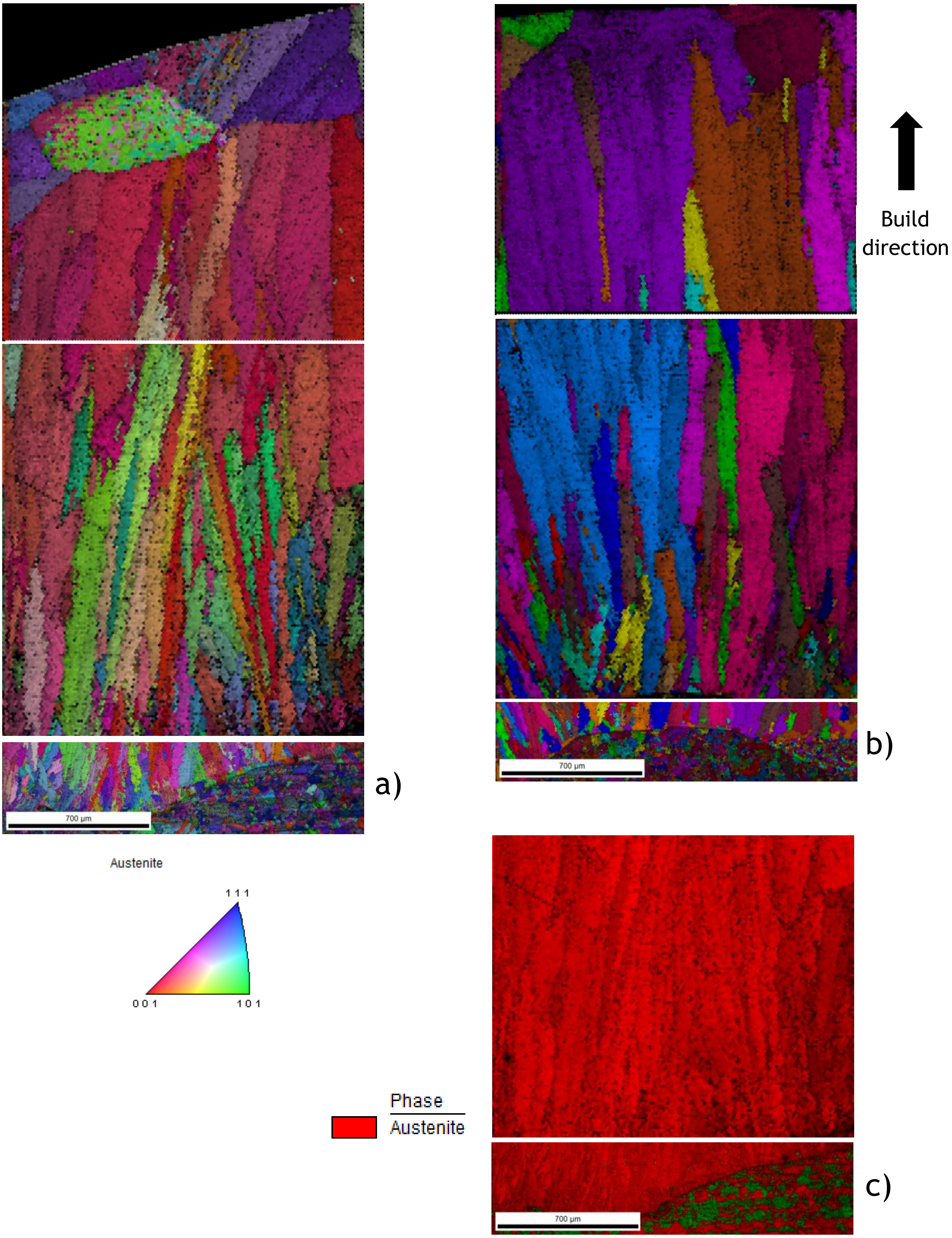

Figure 13. Inverse pole figure map a); grain map b); phase map c); of sample SS [8.5 0.55 5 2] (plate 1, clad 9)

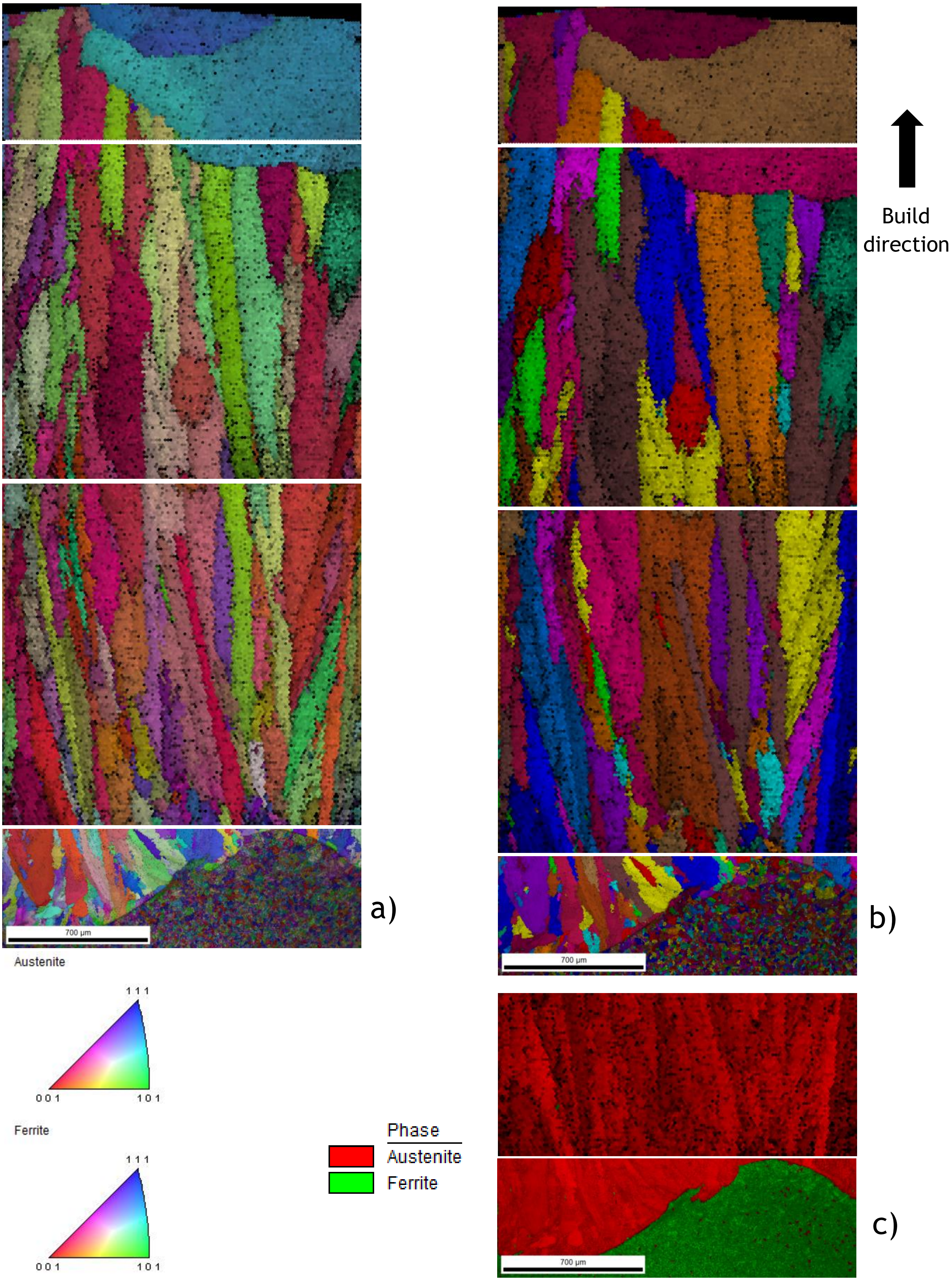

Figure 14. Inverse pole figure map a); grain map b); phase map c); of sample S [8.75 0.55 4.5] (plate 5, clad 1).

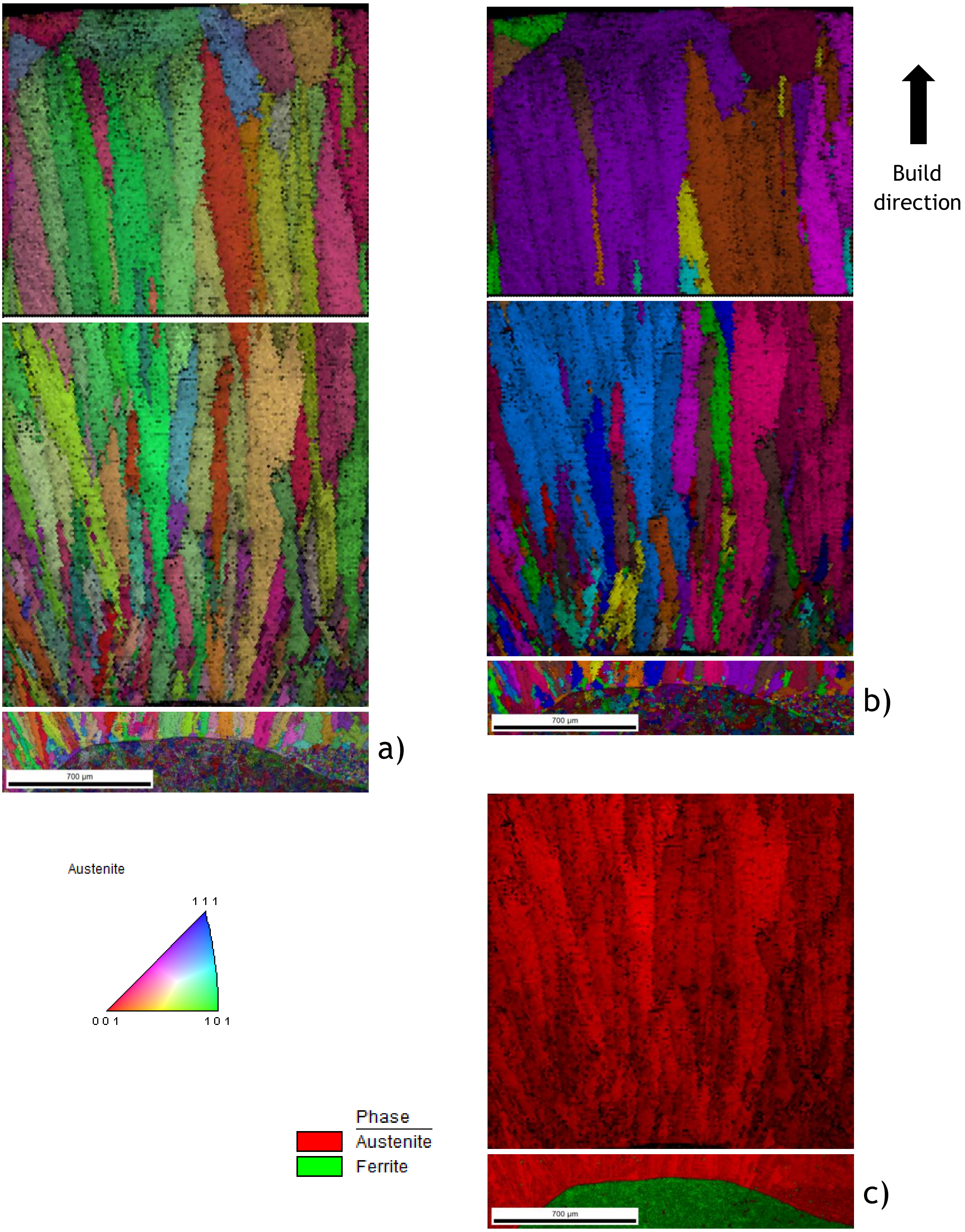

Figure 15. Inverse pole figure map a); grain map b); phase map c); of sample S [9.6 0.6 4.75 4] (plate 5, clad 9).

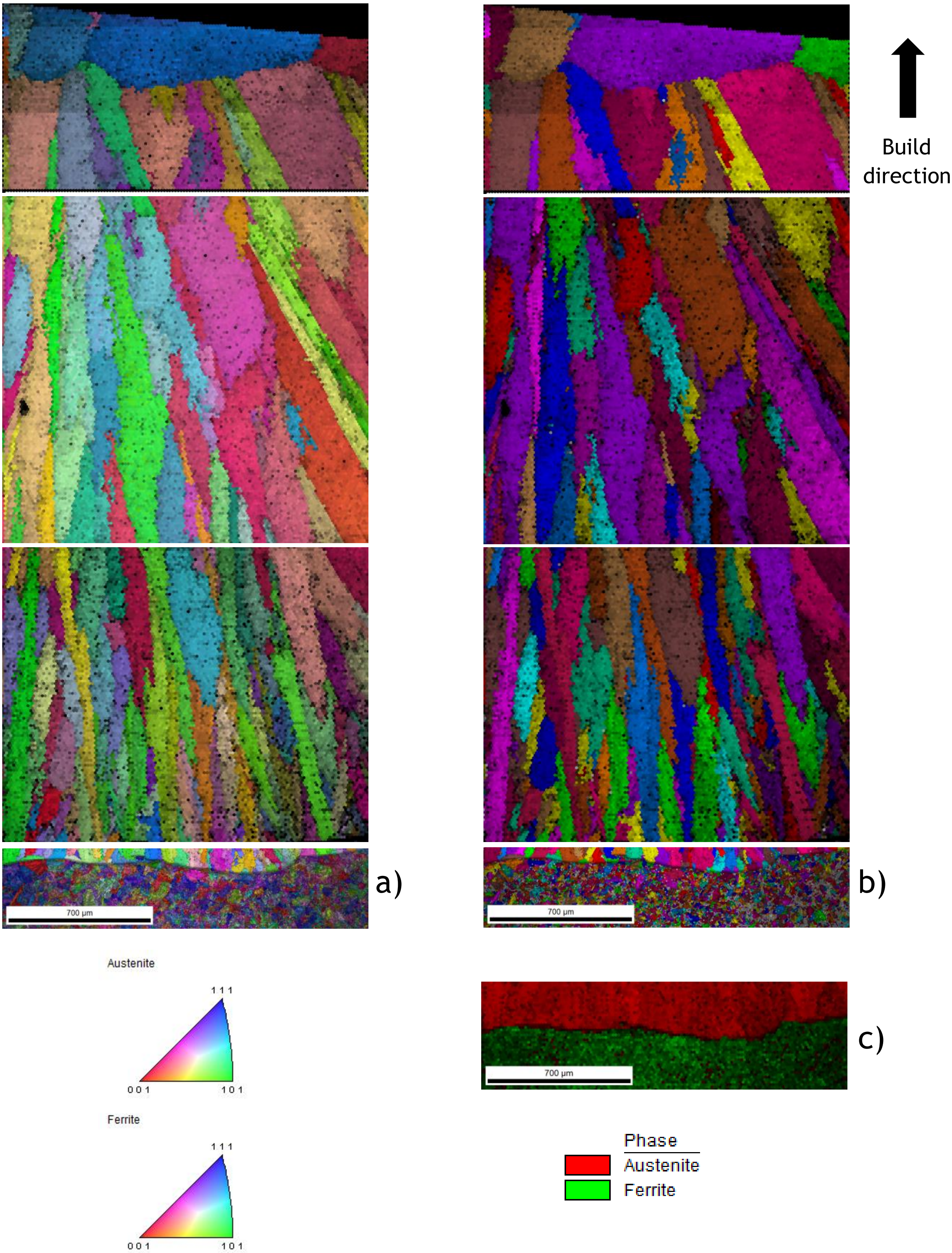

Figure 16. Inverse pole figure map a); grain map b); phase map c); of sample S [9.6 0.6 4.9 4] (plate 6, clad 5).

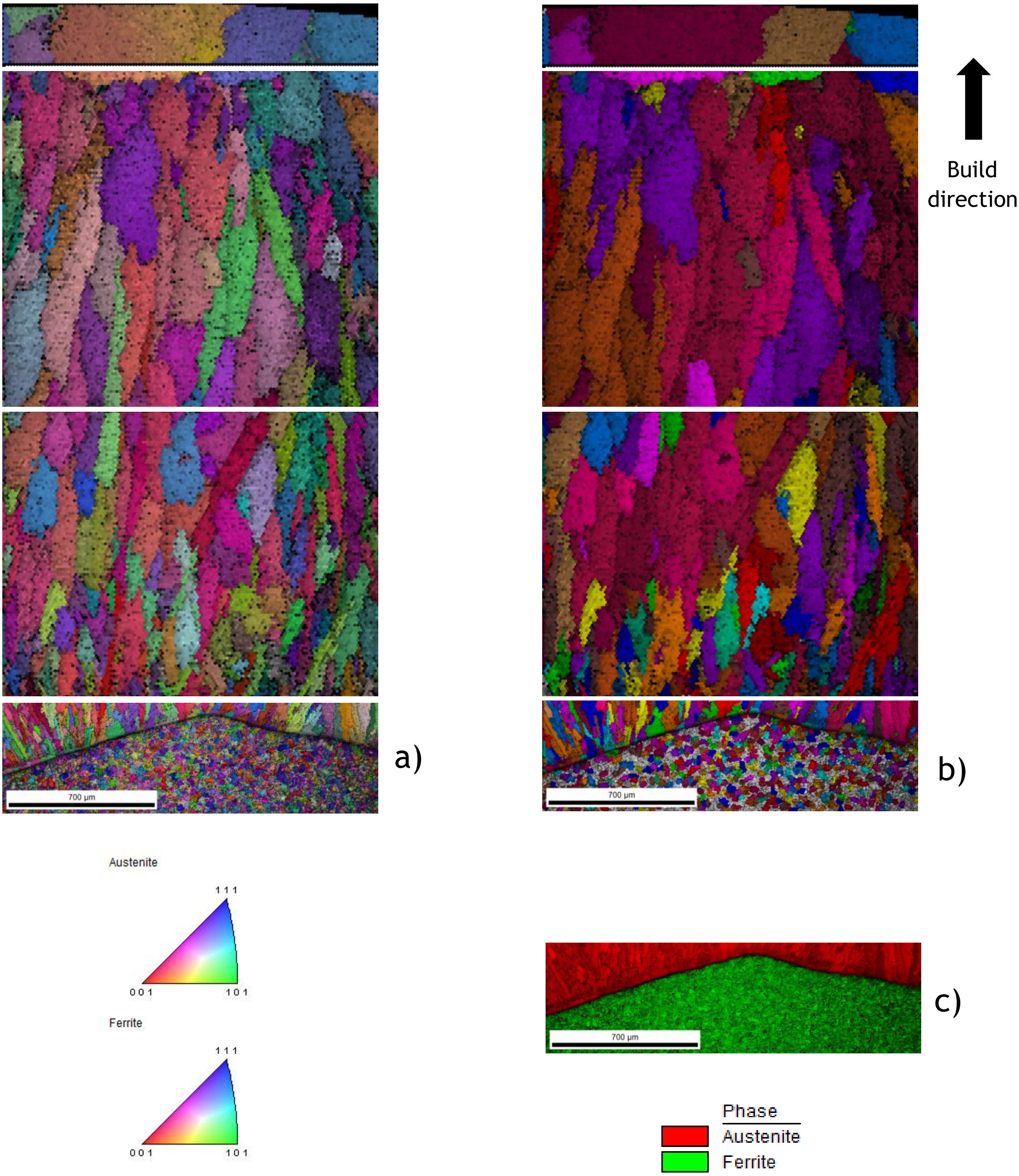

Figure 17. Inverse pole figure map a); grain map b); phase map c); of sample S [9.6 0.6 4.9 4] (plate 6, clad 5) heat treated.

To investigate the influence of substrate material on dilution behaviour, elemental segregation, and microstructural development in Inconel 718 clads produced by Wire Laser Additive Manufacturing (WLAM), two representative samples were analysed: one deposited on 304L stainless steel, SS [8.5 0.5 4 4] (plate 1, clad 1) and the other on S355 structural steel, S [9.6 0.6 4.9 4] (plate 6, clad 5). Backscattered electron (BSE) imaging and energy-dispersive X-ray spectroscopy (EDS) were used to examine four distinct zones in each sample, Figure 18 and Figure 19, with the zones chemical composition represented in Table 8 and Table 9, covering the substrate-clad interface up to the clad region. These zones provide insight into the metallurgical transition, dilution extent, and solidification dynamics across the dissimilar material systems.

In the clad deposited on 304L stainless steel, sample SS [8.5 0.5 4 4] (plate 1, clad 1), the dilution zone near the interface (Z1) showed a typical stainless steel 304L composition. As the analysis moved into the clad (Z2 and Z3), Ni increased steadily, reaching 36.96 wt.% Ni, while Fe decreased to 39.66 wt.%. This progressive compositional shift indicates a smooth transition into the Inconel matrix. Z4 composition, is consistent with the formation of Nb-rich Laves phase—a brittle interdendritic constituent common in additive manufactured Inconel. The presence of this phase is associated to localized elemental enrichment during solidification and is detrimental to ductility if not dissolved during post-processing.

In the sample deposited on S355 structural steel, S [9.6 0.6 4.9 4] (plate 6, clad 5), the compositional gradient was more abrupt. Z1, located in the substrate, exhibited extremely high Fe content (97.84 wt.%) with negligible alloying elements, confirming minimal dilution at that depth. In Z2, the transition region showed a sharp drop in Fe (52.95 wt.%) and a rise in Ni (32.58 wt.%), indicating a metallurgical fusion zone with partial substrate mixing. As with the 304L-based clad, Z4 in this sample also revealed the presence of a strongly segregated Laves phase, with Nb maximum of 58.83 wt.%. The elemental composition and bright BSE contrast confirm this as an interdendritic Nb-rich phase—typical of Laves-type segregation in unrefined as-deposited Inconel 718.

Comparing the two systems, it is evident that the 304L substrate promoted a more gradual dilution gradient due to its similar thermal and metallurgical characteristics relative to Inconel 718. In contrast, the S355 substrate, with its ferritic-pearlitic structure and lower thermal conductivity, produced abrupt transitions and more severe segregation.

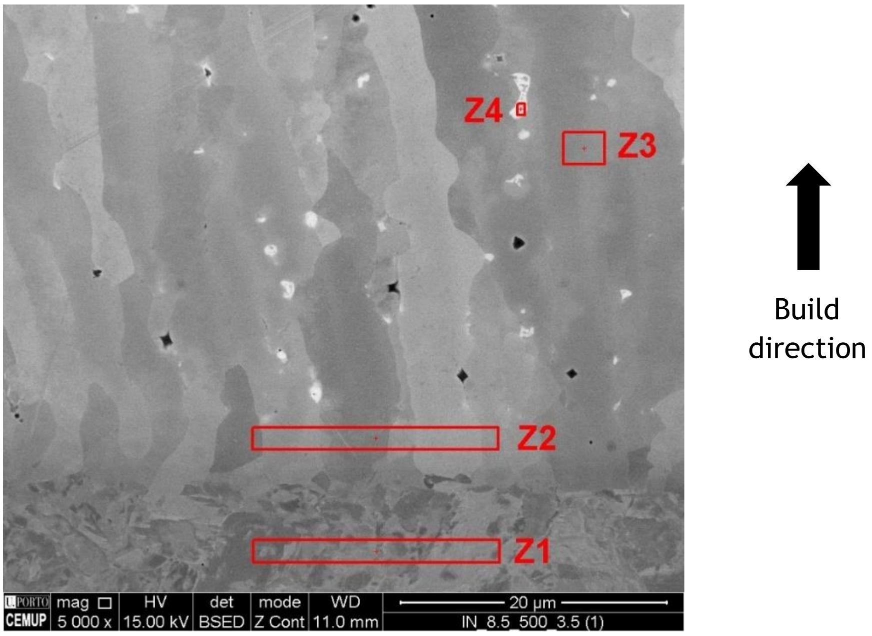

Figure 18. SS [8.5 0.5 4 4] (plate 1, clad 1) interface SEM backscattered electron imaging with zones Z1, Z2, Z3 and Z4 analysed by EDS.

Table 8. Wt.% chemical composition of zones Z1, Z2, Z3 and Z4 obtained by EDS from sample SS [8.5 0.5 4 4] (plate 1, clad 1).

Element	Z1 (Wt.%)	Z2 (Wt.%)	Z3 (Wt.%)	Z4 (Wt.%)
C	0.38	0.43	0.54	0.42
Al		0.37	0.35	
Nb		1.84	1.80	27.78
Mo		1.72	2.12	5.33
Ti		0.42	0.53	2.49
Cr	18.50	17.68	17.77	10.98
Fe	72.12	47.04	39.66	19.61
Ni	8.59	30.00	36.96	32.69
Si	0.42	0.51		0.69
Mn	1.48			

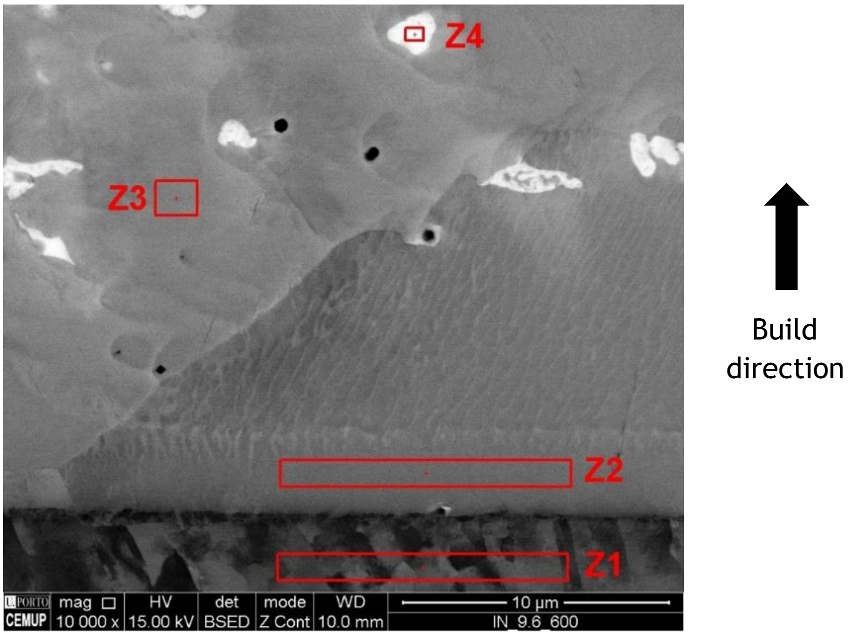

Figure 19. S [9.6 0.6 4,9 4] (plate 6, clad 5) interface SEM backscattered electron imaging with zones Z1, Z2, Z3 and Z4 analysed by EDS.

Table 9. Wt.% chemical composition of zones Z1, Z2, Z3 and Z4 obtained by EDS from sample S [9.6 0.6 4.9 4] (plate 6, clad 5).

Element	Z1 (Wt.%)	Z2 (Wt.%)	Z3 (Wt.%)	Z4 (Wt.%)
C	0.39	0.41	0.58	4.68
Al		0.36	0.33	
Nb		1.34	1.71	58.83
Mo		1.65	2.32	
Ti			0.47	4.97
Cr		0.28	12.68	6.10
Fe	97.84	52.95	43.38	15.12
Ni		32.58	38.44	15.30
Si	0.29			
Mn	1.48			

All the oxide inclusions observed by SEM-EDS in the nickel-based alloy are mainly the inclusions of $MgO{\cdot}Al_2O_3$ spinel core surrounded by (Nb,Ti)CN layer. These oxides can be seen in Figure 20, matching with zones Z9 and Z10 having a chemical composition, presented in Table *10*.

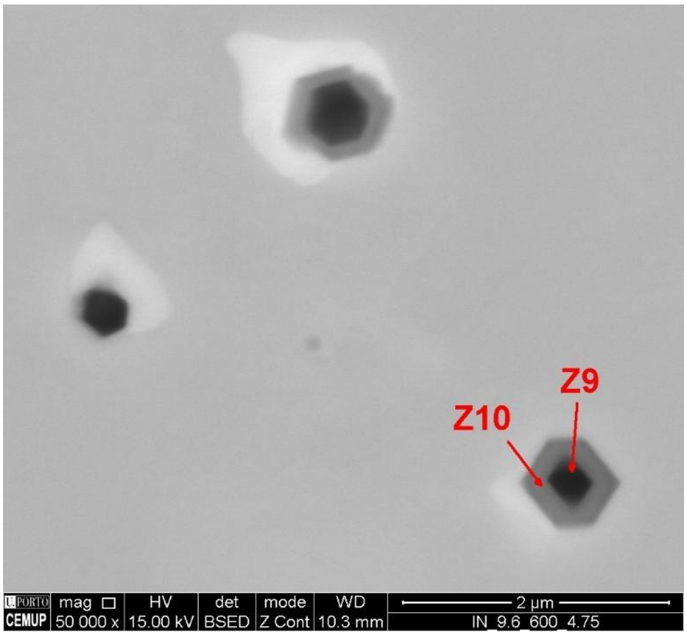

Figure 20. $MgO{\cdot}Al_2O_3$ spinel core surrounded by (Nb,Ti)CN layer, from sample S [9.6 0.6 4.75 4] (plate 5, clad 9).

Table 10. Wt.% chemical composition of zones Z9 and Z10, obtained by EDS from sample S [9.6 0.6 4.9 4] (plate 5 clad 9).

Element	Z9 (Wt.%)	Z10 (Wt.%)
C	0.66	1.24
N		6.06
O	9.05	4.14
Al	7.75	1.34
Nb	21.89	29.73
Mo	2.77	
Ti	17.69	25.48
Cr	7.87	6.34
Fe	14.43	11.45
Ni	16.19	13.93
Mg	1.69	

Laves phase in WLAM Inconel alloys typically precipitates in interdendritic regions due to the segregation of niobium (Nb), molybdenum (Mo), and titanium (Ti) during solidification. These elements are rejected from the solidifying dendrite cores and concentrate in the last regions to solidify, forming localized, solute-enriched zones. As a result, the Laves phase tends to appear along cellular or dendritic boundaries in the as-built microstructure. This is quite visible in Figure 21.

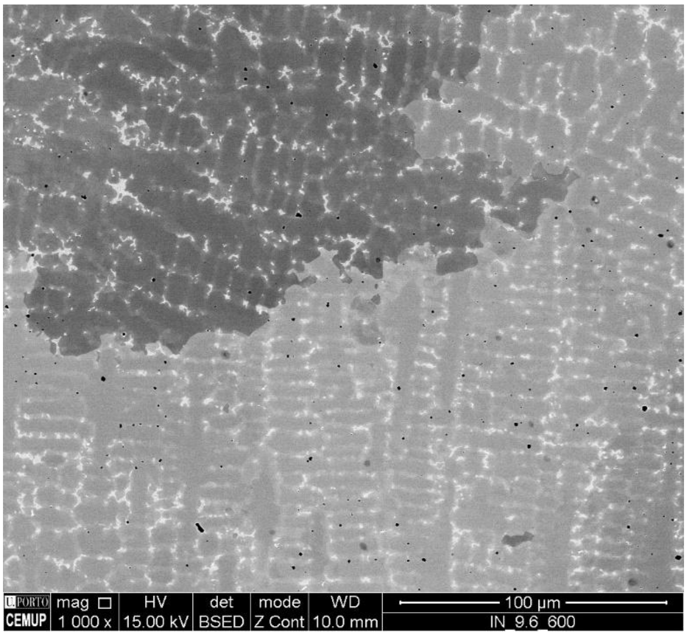

Figure 21. Laves phase distribution in sample S [9.6 0.6 4.9 4] (plate 6, clad 5).

4.3 Hardness Results

Starting the analysis of the hardness results for the samples SS [8.5 0.5 4 4] (plate 1, clad 1), displayed at Table 11 and Figure 22, the clad had an average hardness of 201 HV 0.3, showing small variations throughout the clad, without any hardness variation trend. The substrate had a 192 HV 0.3 average hardness, also without any noticeable trend. As expected, no hardness change was noticed in the HAZ due to SS304L, an austenitic stainless steel with higher thermal stability and corrosion resistance, forming a more stable HAZ with less pronounced microstructural transformations.

Table 11. SS [8.5 0.5 4 4] (plate 1, clad 1) hardness results.

SS [8.5 0.5 4 4] (plate 1, clad 1)	
Clad	201 HV 0.3
Substrate	192 HV 0.3

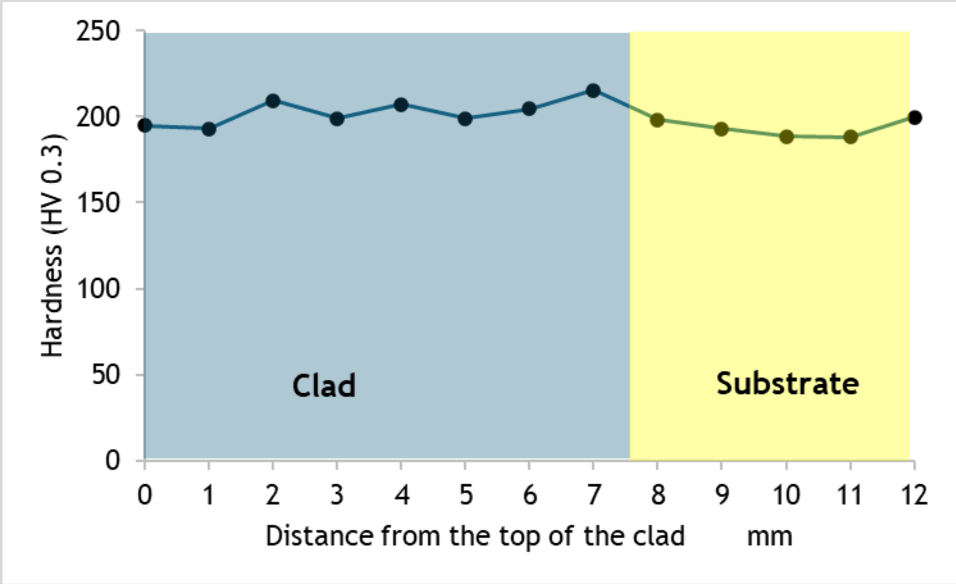

Figure 22. SS [8.5 0.5 4 4] (plate 1, clad 1) hardness profile.

Moving to the analysis of structural steel S355, sample S [9.6 0.6 4.75 4] (plate 5, clad 9), results present in Table 12 and Figure 23, had an average hardness of 225 HV 0.3, also without presenting wide variations or a trend. Different to the 304 stainless steel substrate, S355, a ferritic-pearlitic low-alloy structural steel, exposed to high thermal inputs can lead to grain coarsening, carbide precipitation, and the formation of brittle martensitic or bainitic phases depending on the cooling rate, increasing hardness in the HAZ. This hardness increase was significant, resulting in an increase of 63 Vickers hardness points, in comparison to the substrate with an averaged hardness of 201 HV 0.3. Some effects from the HAZ might still be possible due to the slight negative trend from the hardness of substrate, however, other random harness measurements were performed in the substrate, with similar results to the ones obtained with the hardness profile.

The results of sample S [9.6 0.6 4.75 4] (plate 5, clad 9) with heat treatment, homogenization treatment at 1200 ºC for 15 minutes followed by double aging at 720 ºC 8 hours and 625 ºC 8 hours, are displayed in Table 13 and Figure 24. The most notable was the hardness of the clad, 379 HV 0.3, which is 68% harder than the sample without heat treatment. This could be resulted from precipitation hardening and grain refining. Another change with the heat treatment was the elimination of the brittle HAZ. After heat treatment no harder areas were found near the interface. The harness of the substrate was slightly lower compared to pre heat treated sample, with a hardness of 187 HV 0.3. The hardness 379 HV 0.3 for the heat treated Inconel 718 and 187 HV 0.3 for S355 are within expected values of AMS 5596 (Sheet, Strip, & Plate), and around the limit for S355 expected hardness.

Table 12. S [9.6 0.6 4.75 4] (plate 5, clad 9) hardness results.

S [9.6 0.6 4.75 4] (plate 5, clad 9)	
Clad	225 HV 0.3
HAZ	264 HV 0.3
Substrate	201 HV 0.3

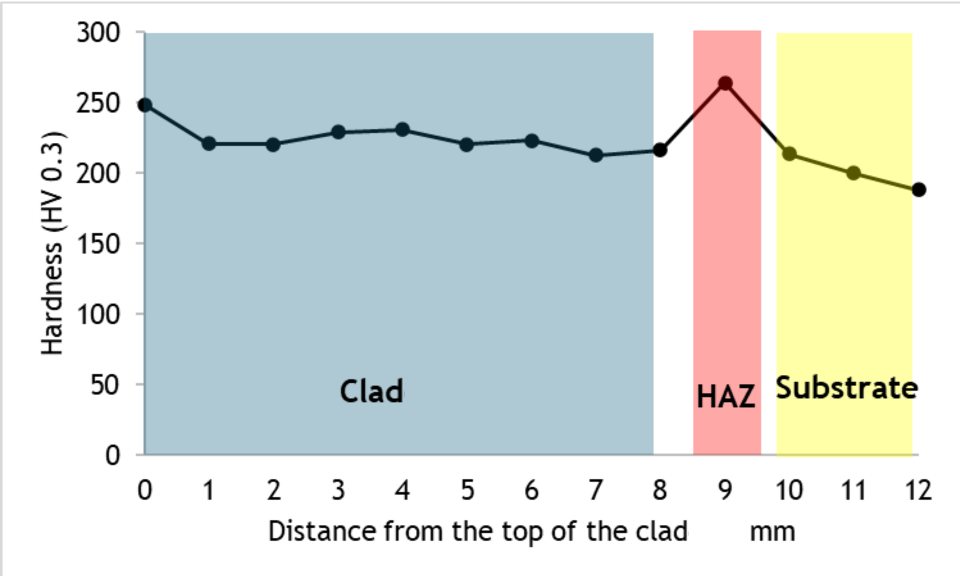

Figure 23. S [9.6 0.6 4.75 4] (plate 5, clad 9) hardness profile.

Table 13. S [9.6 0.6 4.75 4] (plate 5, clad 9) heat treated hardness results.

S [9.6 0.6 4.75 4] (plate 5, clad 9) HT	
Clad	379 HV 0.3
Substrate	187 HV 0.3

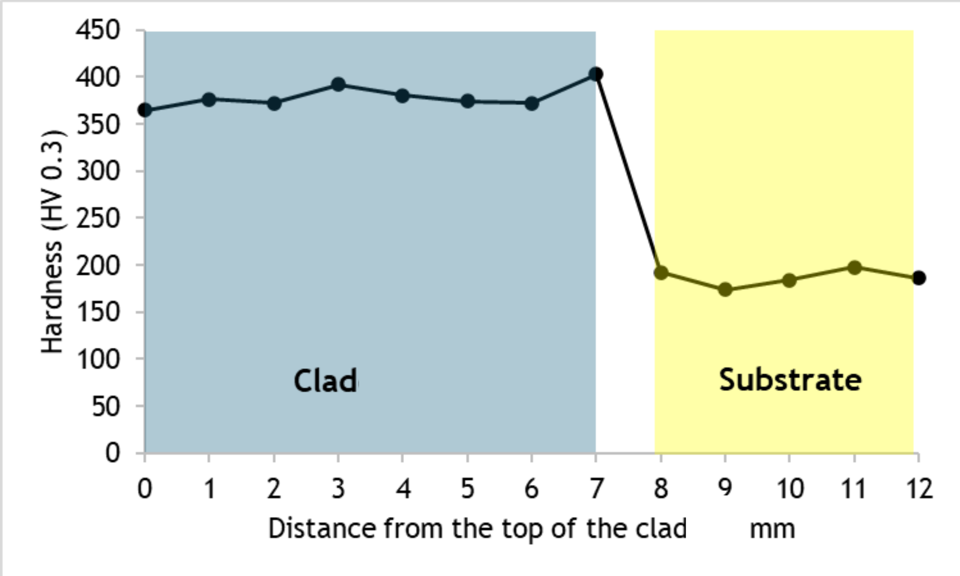

Figure 24. S [9.6 0.6 4.75 4] (plate 5, clad 9) heat treated profile.

Continuing with structural steel S355 substrate, sample S [9.6 0.6 4.9 4] (plate 6, clad 5), displayed at Table 14 and Figure 25, the clad has a hardness of 224 HV 0.3, not presenting major variations or a trend. As for sample S [9.6 0.6 4.75 4] (plate 5, clad 9), a brittle harder HAZ was observed with a hardness of 248 HV 0.3, 54 Vickers hardness points higher than the base material (194 HV 0.3). This harness increased are explained by the reasons explained previously for sample S [9.6 0.6 4.75 4] (plate 5, clad 9).

Sample S [9.6 0.6 4.9 4] (plate 6, clad 5) heat treated, homogenization treatment at 1200 ºC for 10 minutes (5 minutes shorter than in sample S [9.6 0.6 4.75 4] (plate 5, clad 9), followed by double aging at 720 ºC 8 hours and 625 ºC 8 hours, displayed at Table 15 and Figure 26, resulted in a clad with a hardness of 412 HV 0.3, an 84% increase. Due to the homogenization treatment time being shorter than in sample S [9.6 0.6 4.75 4] (plate 5, clad 9), this hardening was more amplified. In this sample, the heat treatment also allowed for the elimination of the brittle.e HAZ. The hardness of the substrate decreased further, from 194 HV 0.3 to 121 HV 0.3.

Table 14. S [9.6 0.6 4.9 4] (plate 6, clad 5) hardness results.

S [9.6 0.6 4.9 4] (plate 6, clad 5)	
Clad	224 HV 0.3
HAZ	248 HV 0.3
Substrate	194 HV 0.3

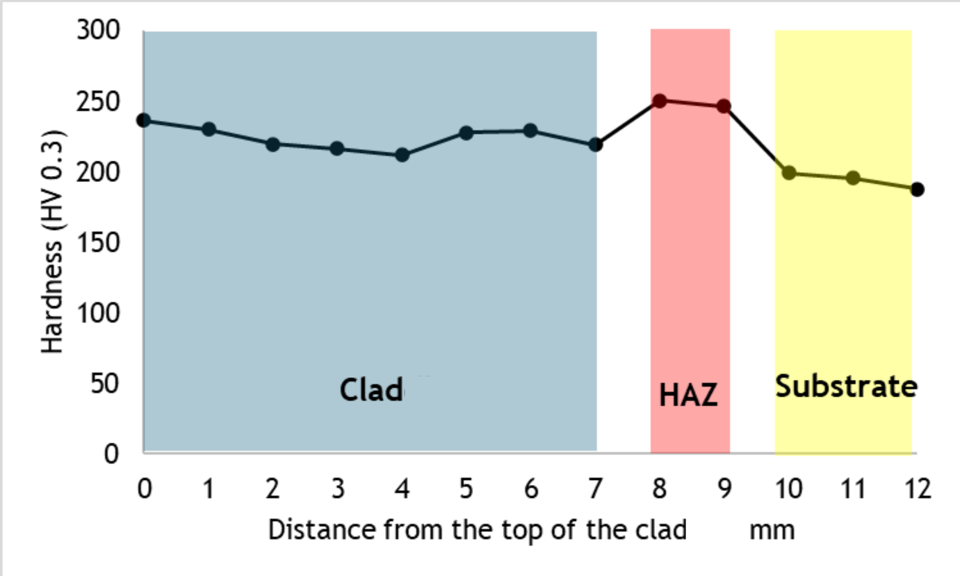

Figure 25. S [9.6 0.6 4.9 4] (plate 6, clad 5) hardness profile.

Table 15. S [9.6 0.6 4.9 4] (plate 6, clad 5) heat treated hardness results.

S [9.6 0.6 4.9 4] (plate 6, clad 5) HT	
Clad	412 HV 0.3
Substrate	121 HV 0.3

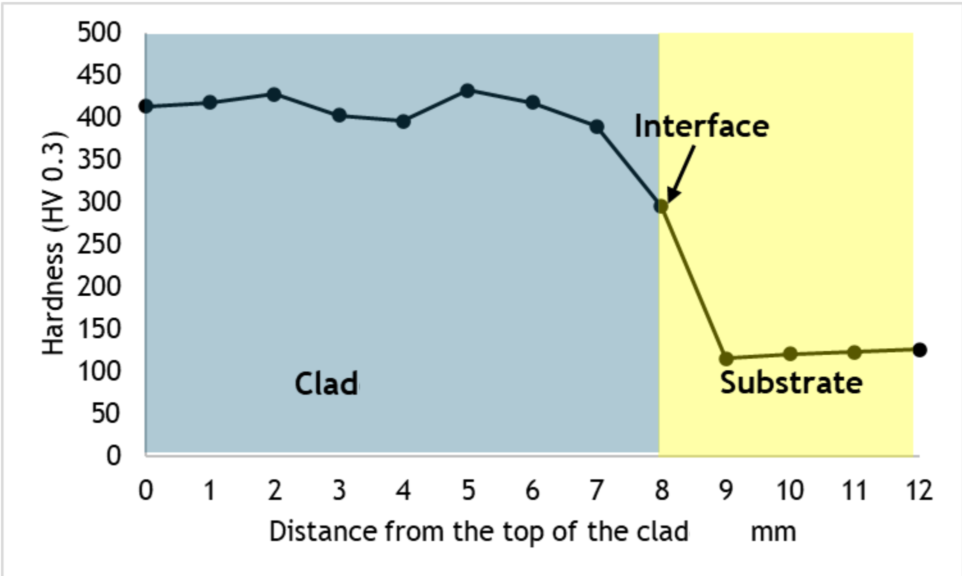

Figure 26. S [9.6 0.6 4.9 4] (plate 6, clad 5) heat treated hardness profile.

4.4 Tensile Test Results

With the goal of performing a mechanical characterization of the Inconel 718 block produced with the same parameters of S [9.6 0.6 4.9 4] (plate 6, clad 5), this block was cut in half, and three specimens were cut from half of the block in each direction: horizontal, vertical and diagonal.

The remainder half of the block was submitted to the treatment described in section 3.3, in order to access the effect of the heat treatment on the mechanical properties the Inconel block.

An example of a specimen post tensile testing can be seen in Figure 27.

Figure 27. Tested tensile specimen.

Starting the analysis with the specimens taken from the block in the horizontal direction, represented in Figure 28, it can be stated that in the as built specimens, the mechanical behaviour was almost identical, the horizontal as built specimens had an $R_{P0.2}$ of 447 ± 9 MPa, R_m of 824 ± 6 and a A of 41 ± 2%. These specimens showed very high ductility but lower mechanical strength, comparable to the annealed properties of Inconel 718, according to ASTM B637 (R_m ~ 860–930 MPa, $R_{p0.2}$ ~ 415–480 MPa and A ≥ 30%).

Moving to heat treated specimens taken from the block in the horizontal direction, the mechanical properties were not as uniform in comparison to the as built specimens, especially specimen H2_TT which had a A of 13%, while the other two specimens had 28% and 33%. This major difference in A was most likely justified by the presence of a major defect where crack propagation becomes critical. The horizontal heat treated specimens had an $R_{P0.2}$ of 853 ± 66 MPa, R_m of 1057 ± 33 and a A of 25 ± 8%. These specimens did not meet all the mechanical strength requirements of ASTM B637, as a R_m ≥ 1240 MPa and $R_{p0.2}$ ≥ 1035 MPa would be expected. As for the A values, the average value was above the 12% specified in ASTM B637, and even the specimen with a subpar result, still fulfilled this criteria. The heat treatment caused an 91% strength increase in $R_{p0.2}$, 28% in R_m and 39% decrease in elongation for the horizontal direction.

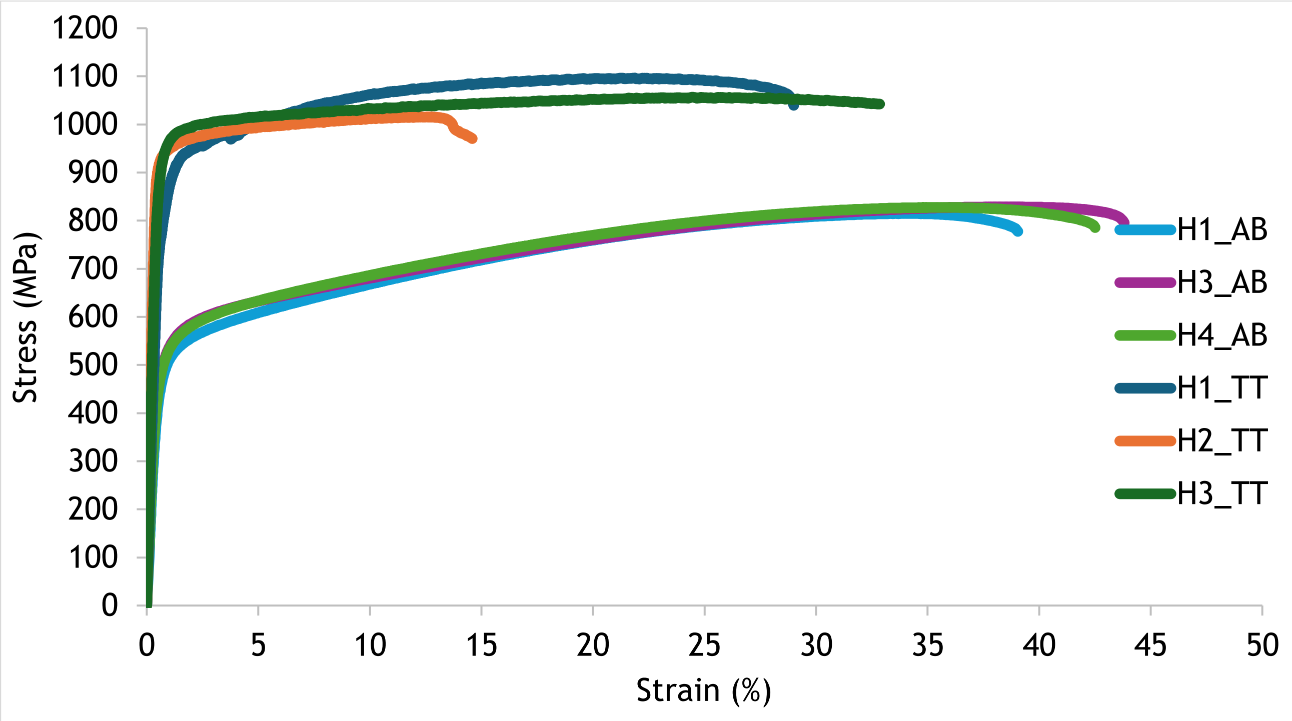

Figure 28. Stress strain curves of horizontal direction specimens.

In the vertical direction, with the tensile tests represented in Figure 29, the as built specimens like in the horizontal direction, showed slight discrepancy. The vertical as built specimens had an $R_{p0.2}$ of 488 ± 8 MPa, R_m of 836 ± 10 and a A of 38 ± 1%. These specimens also showed very high ductility with lower mechanical strength, similar to the annealed properties of Inconel 718, according to ASTM B637.

For the heat treated specimens taken from the block in the vertical direction, the mechanical properties showed only marginal differences. Only two curves are shown for this condition due to one specimen slipping during the tensile test and its removal from the data. The vertical heat treated specimens had an $R_{p0.2}$ of 960 ± 40 MPa, R_m of 1090 ± 33 and a A of 22 ± 0.5%. These specimens also did not meet the mechanical strength requirements of ASTM B637 (R_m ≥ 1240 MPa and $R_{p0.2}$ ≥ 1035 MPa). The elongation values were 83% higher than the 12% specified in ASTM B637. The heat treatment caused an 97% increase in $R_{p0.2}$, 30% in R_m and 42% decrease in elongation for the vertical direction.

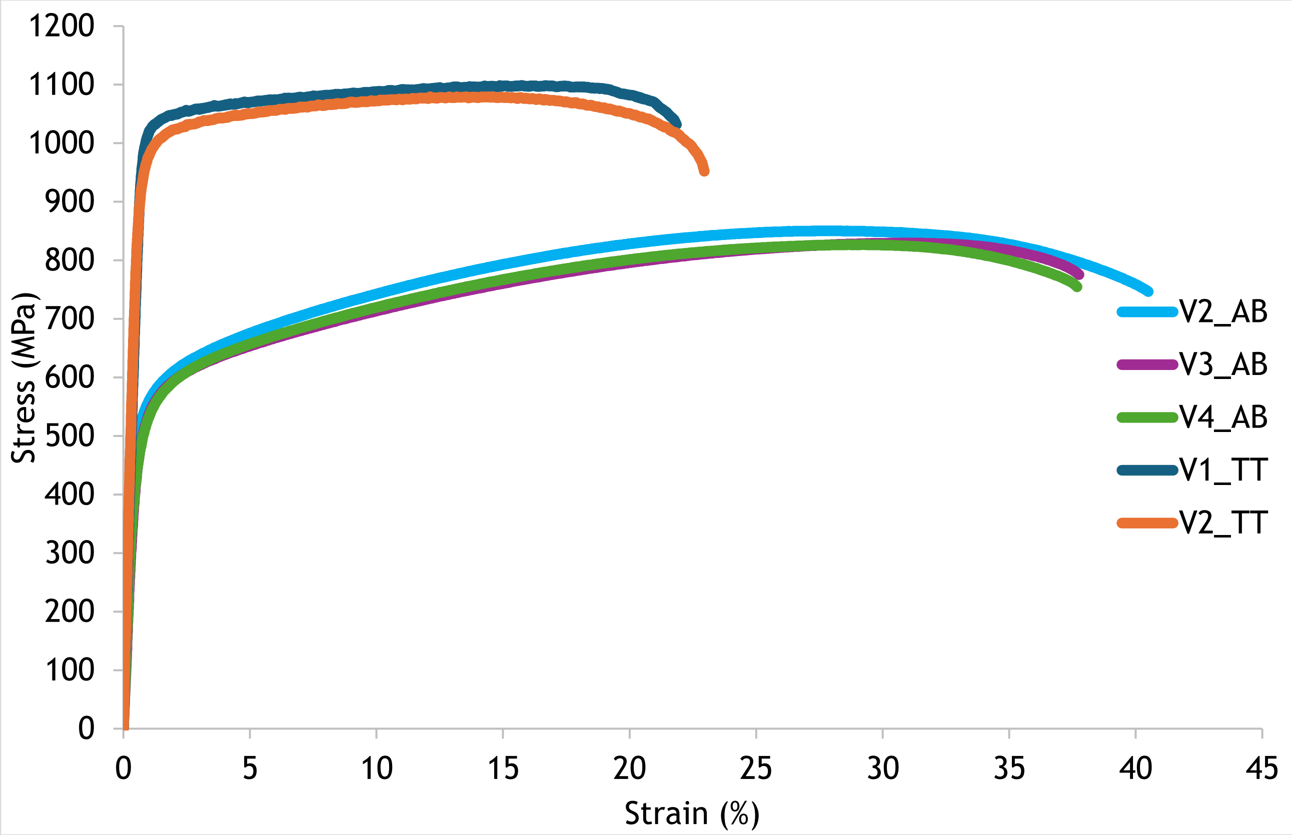

Figure 29. Stress strain curves of vertical direction specimens.

Finally for the diagonal direction, with the tensile curves showed in Figure 30, the as built specimens unlike in the horizontal and vertical direction, there was discrepancy. The curve corresponding to specimen D1_AB had a considerably higher $R_{P0.2}$ of 700 MPa, while D2_AB and D4_AB had an $R_{p0.2}$ of 490 and 510 MPa, respectively. One possible reason for this behaviour can be the position from where the specimen was cut from the block, and if this was one of the first specimens to be cut due to being close to one of the walls of the block, where the cooling is faster, resulting in a more refined grain. Other probable cause is the accumulation of internal stress in the specimen, due to handling, exacerbated by the very thin section of the specimens. The diagonal as built specimens had an average $R_{p0.2}$ of 567 ± 95 MPa, R_m of 883 ± 12 and a A of 28 ± 1%. These specimens also showed high ductility, however lower in comparison to the horizontal and vertical direction specimens.

For the heat treated specimens taken from the block in the diagonal direction, the $R_{P0.2}$ and R_m values comparable between the three specimens, however that was not the case for the elongation, varying from 10% to 19%, to be noted that specimen D1_TT was the only one not fulfilling the 12% elongation required by ASTM B637. The diagonal heat treated specimens had an average $R_{p0.2}$ of 957 ± 2 MPa, R_m of 1116 ± 22 and a A of 14 ± 3%. These specimens also did not meet the mechanical strength requirements of ASTM B637 (Rm ≥ 1240 MPa and $R_{p0.2}$ ≥ 1035 MPa). The elongation values are barely above the 12% specified in ASTM B637. The heat treatment resulted in an 69% increase in $R_{p0.2}$, 26% in R_m and 50% decrease in elongation for the vertical direction.

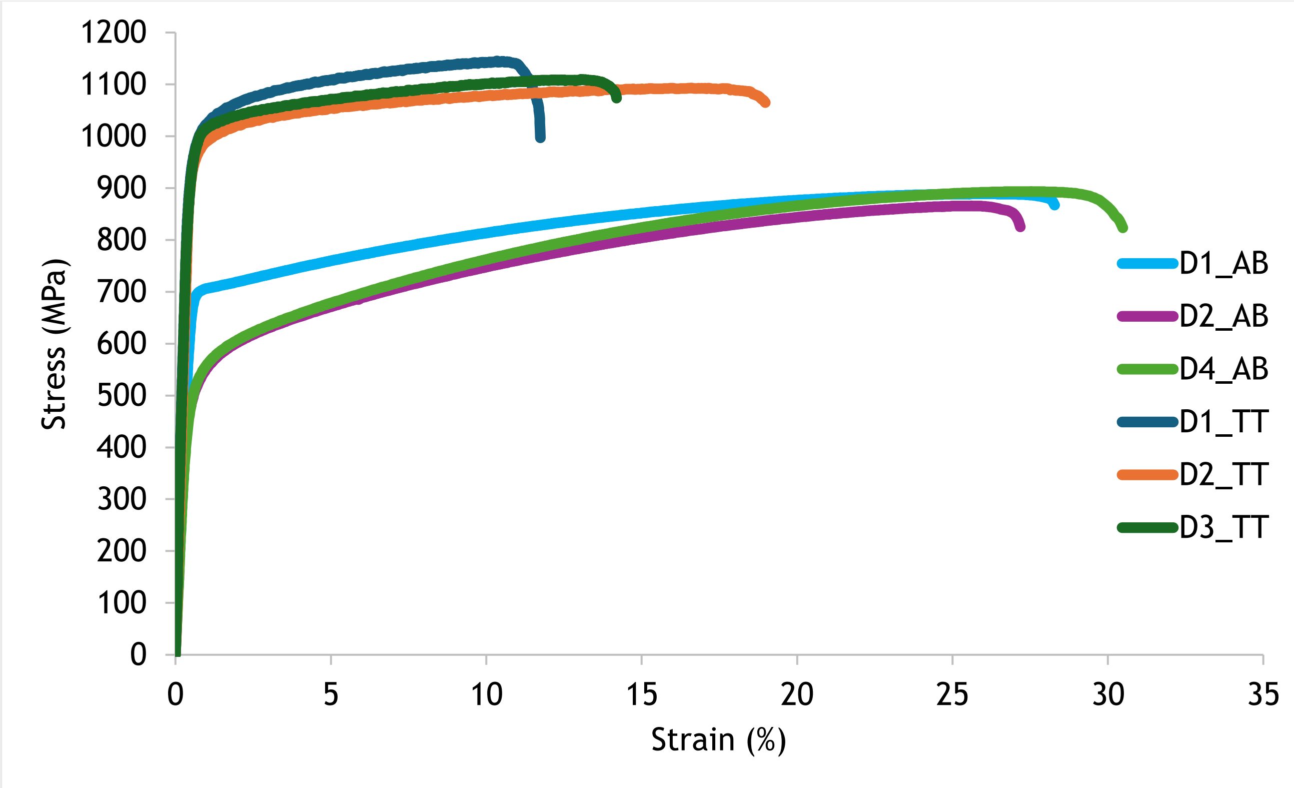

Figure 30. Stress strain curves of diagonal direction specimens.

Table 16 and Table 17 had a summary of the average values of $R_{p0.2}$, R_m, and A (%) for all three directions, for as built and heat treated specimens. Figure 31 contains a representative curve from each condition in order to give a visual representation of the effects of each conditions on the mechanical properties.

In WLAM, mechanical anisotropy is a common and expected characteristic due to the layer-by-layer deposition, thermal history, and epitaxial grain growth that occur during fabrication. One notable manifestation of this anisotropy is the variation in elongation at fracture across different build orientations [76,77].

Specifically, specimens extracted in the horizontal direction (parallel to the layers) typically exhibited higher elongation, while those in the vertical direction (build direction) showed moderate values, and diagonal specimens often performed the worst in terms of ductility. The underlying cause lies in the columnar grain structure that forms during solidification. These grains are aligned along the build direction, growing epitaxially from the substrate through each deposited layer. When tensile loading is applied horizontally, across the grain columns, plastic deformation is better accommodated by dislocation motion and grain boundary sliding. In contrast, vertical loading aligns with the grain direction, making the material more prone to intergranular cracking and less capable of deforming plastically. This is visible by checking that both in as built and heat treated specimens, the highest elongation values are obtained from the horizontal direction [76,77].

The lowest elongation in diagonal specimens likely resulted from a combination of stress orientation and complex grain boundary interactions. Since these specimens are loaded at an angle to the grain structure, they are more likely to encounter mixed-mode failure mechanisms, including both intergranular and transgranular cracking, leading to earlier onset of necking and failure. From the values obtained this point is clear, for both as built and heat treated conditions, the diagonal direction had a substantially lower elongation [76,77].

Table 16. As built tensile results.

	$R_{p0.2}$ (MPa)	R_m (MPa)	A (%)
Horizontal AB	447	824	41
Vertical AB	488	836	38
Diagonal AB	567	883	28

Table 17. Heat treated tensile results.

	$R_{p0.2}$ (MPa)	R_m (MPa)	A (%)
Horizontal HT	853	1057	25
Vertical HT	960	1090	22
Diagonal HT	957	1116	14

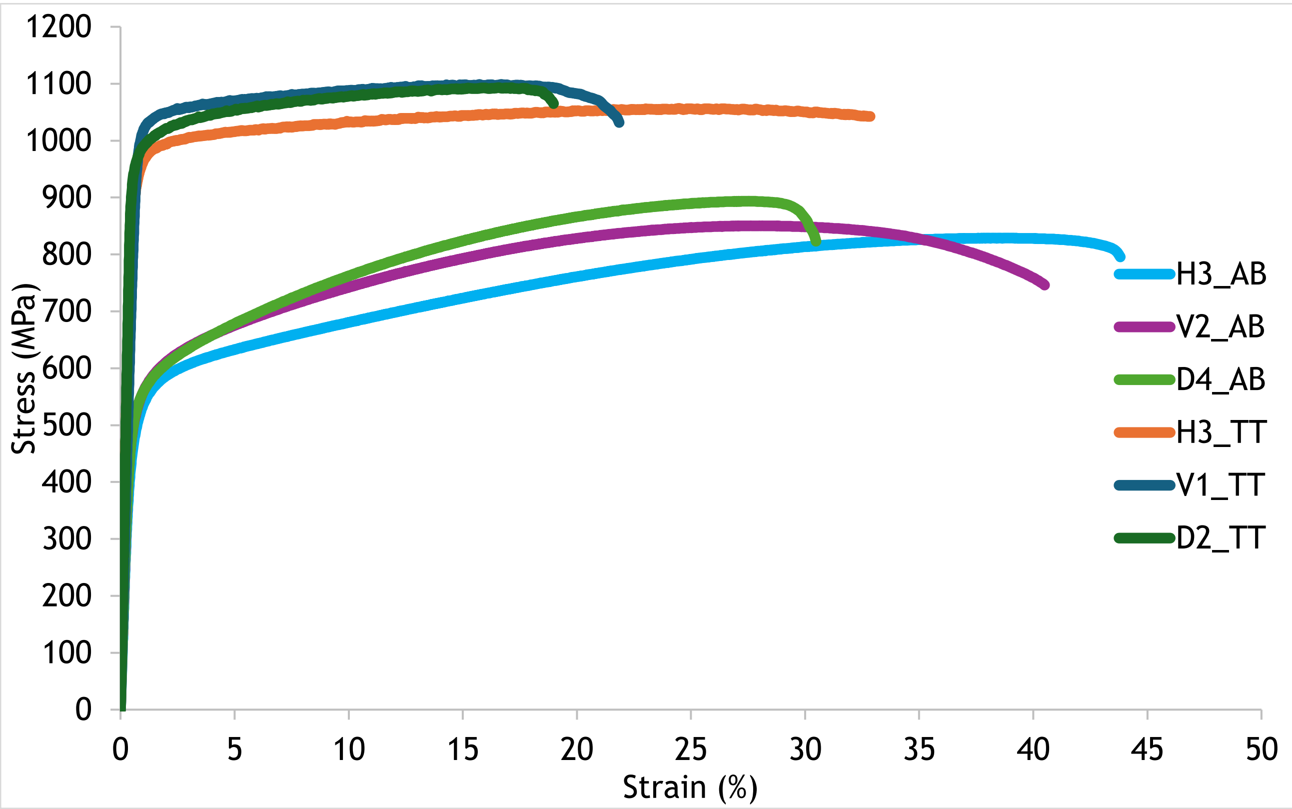

Figure 31. Representative tensile results.

5. Conclusions

This study comprehensively investigated the optimization of Inconel 718 clads produced via Wire Laser Additive Manufacturing (WLAM) on stainless steel 304L and structural steel S355, and, elucidating critical relationships between process parameters, microstructural evolution, mechanical performance, and the effectiveness of targeted post-processing heat treatments.

An extensive parametric investigation was carried out, systematically examining combinations of laser power, laser scanning speed, wire feed rate, and shielding gas pressure. For the 304L stainless steel substrate, clads produced at laser powers above 8.5 kW consistently exhibited higher porosity and cracking, suggesting a critical threshold where excessive energy input compromises clad quality. Laser scanning speeds above 0.55 m/min similarly led to increased defects, emphasizing that moderate scanning speeds are crucial to achieving balanced dilution and minimized porosity. Among shielding gas pressures tested (2, 3, and 4 bar), both 2 bar and 4 bar yielded favourable results, indicating a flexible operational window, although 3 bar produced inconsistent outcomes, likely influenced by other overlapping factors like laser speed.

For S355 structural steel substrates, higher laser powers around 9.6 kW combined with slightly faster laser speeds (0.6 m/min) and elevated wire feed rates (4.75–4.9 m/min) resulted in better clad integrity, demonstrating the necessity of higher thermal inputs to adequately melt and fuse with this substrate. However, the reproducibility of optimal conditions required fine-tuning; notably, subtle variations such as decreasing the wire feed rate from 4.9 to 4.75 m/min were shown to improve reliability and consistency of results. Conversely, moderate laser powers (around 8.75 kW) produced acceptable clads but showed a 50% success rate regarding defect formation and wettability, highlighting the sensitivity of this substrate to small parameter deviations. Shielding gas pressure at 4 bar proved consistently beneficial for S355, with lower pressures failing to maintain proper melt pool protection and higher dilution consistency.

Detailed microstructural characterization via SEM, EBSD, and EDS analyses provided scientific validation for observed trends. The stainless steel 304L substrate demonstrated smoother dilution gradients due to improved metallurgical compatibility with Inconel 718, facilitating more homogeneous interdiffusion of elements. In contrast, structural steel S355 exhibited sharper dilution interfaces, attributed to substantial thermal conductivity differences and alloying incompatibilities, which resulted in pronounced hardness increases (up to 264 HV 0.3) in the Heat-Affected Zone (HAZ). These findings emphasize the necessity of precise control over thermal gradients during WLAM deposition on structural steels.

The inherent microstructural anisotropy induced by the WLAM process manifested through pronounced columnar grain structures, accompanied by Nb-rich Laves phase segregation in interdendritic regions, significantly compromising ductility and toughness. A post-deposition heat treatment—homogenization at 1200°C followed by double aging at 720°C and 620°C was performed to address these issues, dissolving detrimental Laves phases, refining grain morphologies, and notably reducing brittleness in the HAZ. Consequently, the hardness of clads significantly increased from approximately 225 HV 0.3 to 412 HV 0.3, representing an 84% improvement.

Mechanical evaluations through tensile testing underscored the efficacy of the applied heat treatments, with substantial increases in $R_{P0.2}$ observed across all tested directions: horizontally (447 MPa to 853 MPa), vertically (488 MPa to 960 MPa), and diagonally (567 MPa to 957 MPa). Tensile strength (R_m) similarly improved, increasing horizontally (824 MPa to 1057 MPa), vertically (836 MPa to 1090 MPa), and diagonally (883 MPa to 1116 MPa). However, significant anisotropy persisted, particularly evident in elongation (A) reductions after heat treatment—horizontally (41% to 25%), vertically (38% to 22%), and diagonally (28% to 14%)—highlighting the strong dependency of mechanical properties on grain orientation and build direction.

These comprehensive findings hold substantial implications for industrial sectors requiring high-performance materials, such as aerospace, energy-generation systems, like nuclear, and petrochemical equipment. Through detailed optimization of deposition parameters and tailored heat treatments, this research demonstrates clear pathways for enhancing cladding integrity, prolonging service life, and reducing manufacturing costs.

In summary, this thesis provides a scientifically robust foundation and practical guidelines for the successful implementation and industrial integration of WLAM processes for Inconel 718 clads, emphasizing meticulous control over deposition parameters, careful substrate selection, targeted microstructural manipulation, and effective heat-treatment protocols to achieve reliable, high-performance coatings suitable for demanding applications.

6. Future Work

To build upon the findings of this study, future work should include a more detailed analysis across the depth of the cladding, to have a full understanding along the length of the clad.

Additionally, post-deposition heat treatments should be performed in vacuum or controlled atmospheres , as some defects may be attributable to oxidation or uncontrolled gas interactions during furnace exposure. Implementing an inert or reduced-oxygen environment could minimize surface contamination and improve the effectiveness of homogenization and phase precipitation.

Finally, there is strong potential for the development of machine learning frameworks trained on experimental datasets—including process parameters, geometry metrics, microstructural features, and mechanical properties—to accelerate the optimization of WLAM cladding conditions. By integrating such models with real-time process monitoring data, future systems could autonomously predict defect formation, adapt deposition strategies on-the-fly, and ensure consistent quality in complex geometries or dissimilar material systems. These data-driven approaches represent a critical step toward the industrial-scale deployment of WLAM.

References

1. Seow, C.E., Coules, H.E., Wu, G., Khan, R.H.U., Xu, X., Williams, S. Wire + Arc Additively Manufactured Inconel 718: Effect of post-deposition heat treatments on microstructure and tensile properties. Mater. Des. 2019, 183, 108157.

2. Huang, W., Chen, S., Xiao, J., Jiang, X., Jia, Y. Laser wire-feed metal additive manufacturing of the Al alloy. Opt. Laser Technol. 2020, 106627.

3. Wen, P., Wang, G., Chen, Y. Effect of laser scanning and powder addition on microstructure and mechanical properties for hot-wire-feed laser additive manufacturing. J. Laser Appl. 2017, 29(2), 022302.

4. Sun, Z., Kuo, M. Bridging the joint gap with wire feed laser welding. J. Mater. Process. Technol. 1999, 87(1–3), 213–222.

5. Akhter, R., et al. Review on Laser-Based Additive Manufacturing of Nickel-Based Superalloys. Materials 2021, 14(2), 456.

6. Sames, W.J., et al. The Metallurgy and Processing Science of Metal Additive Manufacturing. Int. Mater. Rev. 2016, 61(5), 315–360.

7. Rong, Y., et al. Microstructural Evolution and Mechanical Properties of Inconel 718 Deposited on Stainless Steel by DED. Surf. Coat. Technol. 2020, 397, 125958.

8. DebRoy, T., et al. Additive Manufacturing of Metallic Components – Process, Structure and Properties. Prog. Mater. Sci. 2018, 92, 112–224.

9. Muthu, S.S., Savalani, M.M. Handbook of Sustainability in Additive Manufacturing. Springer, 2016.

10. Gibson, I., Rosen, D.W., Stucker, B. Additive Manufacturing Technologies: 3D Printing, Rapid Prototyping, and Direct Digital Manufacturing. 3rd ed. Springer, 2021.

11. Ngo, T.D., et al. Additive manufacturing (3D printing): A review of materials, methods, applications and challenges. Compos. B Eng. 2018, 143, 172–196.

12. Thompson, M.K., et al. Design for Additive Manufacturing: Trends, opportunities, considerations, and constraints. CIRP Ann. 2016, 65(2), 737–760.

13. Ventola, C.L. Medical Applications for 3D Printing: Current and Projected Uses. Pharm. Ther. 2014, 39(10), 704–711.

14. Ford, S., Despeisse, M. Additive manufacturing and sustainability: An exploratory study of the advantages and challenges. J. Clean. Prod. 2016, 137, 1573–1587.

15. Huang, R., et al. Energy and emissions saving potential of additive manufacturing: the case of lightweight aircraft components. J. Clean. Prod. 2016, 135, 1559–1570.

16. Baumers, M., et al. Energy inputs to additive manufacturing: Does capacity utilization matter? Proc. Inst. Mech. Eng. B J. Eng. Manuf. 2011, 225(12), 2228–2236.

17. Zhang, Y., et al. Build path planning for additive manufacturing: A review of current methodologies and future directions. Int. J. Adv. Manuf. Technol. 2017, 95, 2281–2295.

18. Gibson, I., Rosen, D.W., Stucker, B. Additive Manufacturing Technologies. 3rd ed. Springer, 2021.

19. Herzog, D., et al. Additive manufacturing of metals. Acta Mater. 2016, 117, 371–392. https://doi.org/10.1016/j.actamat.2016.07.019

20. Coatings. State of the Art in Directed Energy Deposition: From Additive Manufacturing to Materials Design. Coatings 2019, 9(7), 418. https://doi.org/10.3390/coatings9070418

21. Int. J. Therm. Sci. Numerical simulation of heat and mass transfer in laser directed energy deposition. Int. J. Therm. Sci. 2024. https://doi.org/10.1016/j.ijthermalsci.2024.106954

22. J. Laser Appl. Advances in the modeling of laser direct metal deposition. J. Laser Appl. 2019, 27(S1), S15001. https://doi.org/10.2351/1.5066721

23. ArXiv. Molten pool characteristics of a nickel-titanium shape memory alloy for directed energy deposition. 2021.

24. Menon, N., Basak, A. Multi-fidelity surrogate with heterogeneous input spaces for modeling melt pools in laser-directed energy deposition. ArXiv, 2024.

25. Chadha, D. Directed Energy Deposition via Artificial Intelligence Enabled Approaches. Complexity 2022, 2767371. https://doi.org/10.1155/2022/2767371

26. Int. J. Mech. Sci. A comprehensive analytical-computational model of laser directed energy deposition to predict deposition geometry and integrity for sustainable repair. Int. J. Mech. Sci. 2021, 211, 106790. https://doi.org/10.1016/j.ijmecsci.2021.106790

27. Manufacturing. A Review on Wire-Fed Directed Energy Deposition Based Metal Additive Manufacturing. Manufacturing 2019, 7(1), 45. https://doi.org/10.3390/manufacturing7010045

28. Shah, A., et al. A review of the recent developments and challenges in wire arc additive manufacturing (WAAM) process. J. Manuf. Mater. Process. 2023, 7(3), 97. https://doi.org/10.3390/jmmp7030097

29. Jin, W., et al. Wire Arc Additive Manufacturing of Stainless Steels: A Review. Appl. Sci. 2020, 10(5), 1563. https://doi.org/10.3390/app10051563

30. Liu, J., et al. Wire and arc additive manufacturing of metal components: a review of recent research developments. Int. J. Adv. Manuf. Technol. 2020, 111(1–2), 149–198. https://doi.org/10.1007/s00170-020-05966-8

31. Heralić, A., Christiansson, A.K., Lennartson, B. Height control of laser metal-wire deposition. Mechatronics 2012, 22(3), 408–418.

32. Frazier, W.E. Metal Additive Manufacturing: A Review. J. Mater. Eng. Perform. 2014, 23, 1917–1928.

33. Toyserkani, E., Khajepour, A., Corbin, S.F. Laser Cladding. CRC Press, 2004.

34. Williams, S.W., et al. Wire + Arc Additive Manufacturing. Mater. Sci. Technol. 2016, 32(7), 641–647.

35. Gharbi, M., Mumtaz, K., Reza, S., Hopkinson, N. Evaluation of process parameters and mechanical properties for DED of Inconel 718. Mater. Sci. Eng. A 2016, 667, 511–520.

36. Thompson, S.M., Bian, L., Shamsaei, N., Yadollahi, A. An overview of Direct Laser Deposition for metal additive manufacturing. Addit. Manuf. 2015, 8, 36–62.

37. Koseki, T., Yamamoto, N., Matsuda, N. Grain refinement by laser scanning in DED. Metals 2020, 10(2), 273.

38. Ma, J., Ma, C., Zhang, Y. Process control in wire-laser DED for improved microstructure and mechanical properties. Addit. Manuf. 2020, 37, 101723.

39. Song, X., Pan, Z., Cuiuri, D., Ding, D. Thermal control and path optimization in WLAM of stainless steel. J. Mater. Process. Technol. 2022, 299, 117319.

40. Sims, C.T., Stoloff, N.S., Hagel, W.C. Superalloys II: High-Temperature Materials for Aerospace and Industrial Power. Wiley, 1987.

41. Reed, R.C. The Superalloys: Fundamentals and Applications. Cambridge Univ. Press, 2006.

42. Eiselstein, F.A. Metallurgy of a columbium-hardened nickel-chromium-iron alloy. Adv. Mater. Res. 1965, 1, 121–148.

43. Donachie, M.J., Donachie, S.J. Superalloys: A Technical Guide. 2nd ed. ASM Int., 2002.

44. Lippold, J.C., Kiser, S.D. Welding Metallurgy and Weldability of Nickel-Base Alloys. Wiley, 2011.

45. Zhang, Y., Liu, S., Wang, L. Microstructure and mechanical properties of Inconel 718 fabricated by laser-wire DED. J. Mater. Process. Technol. 2019, 270, 216–225.

46. Thapliyal, S., Shukla, M., Dinda, G.P. Effect of post-processing on microstructure and hardness of wire laser additive manufactured Inconel 718. Addit. Manuf. 2021, 38, 101822.

47. Lu, Y., Ma, Y., Lin, X. Influence of ultrasonic-assisted DED on the microstructure of Inconel 718. Mater. Des. 2020, 194, 108934.

48. Sahasrabudhe, H., Bandyopadhyay, A. Laser additive manufacturing of Inconel 718: Microstructure evolution and mechanical properties. Addit. Manuf. 2016, 5, 1–12.

49. Toyserkani, E., Khajepour, A., Corbin, S.F. Laser Cladding. CRC Press, 2004.

50. Wu, X., Liang, J., Mei, J., Mitchell, C., Goodwin, P.S., Voice, W. Microstructure and performance of laser deposited Ti-6Al-4V. Mater. Des. 2004, 25(7), 603–609.

51. Pinkerton, A.J. Laser direct metal deposition: theory and application. Laser Appl. Surf. Modif. 2007, 333–360.

52. Davis, J.R. Structural Materials for Power Generation. ASM Int., 2000.

53. Sedriks, A.J. Corrosion of Stainless Steels. John Wiley & Sons, 1996.

54. Lippold, J.C., Kotecki, D.J. Welding Metallurgy and Weldability of Stainless Steels. Wiley-Interscience, 2005.

55. Reed, R.C. The Superalloys: Fundamentals and Applications. Cambridge Univ. Press, 2006.

56. Liu, J., et al. Functionally graded materials by laser metal deposition: Design, microstructure, and properties. Mater. Sci. Eng. A 2019, 766, 138360.

57. Ma, J., Zhao, J., Zhang, H., et al. Microstructural evolution and mechanical behavior of Inconel 718 wire-laser claddings on low alloy steel substrate. Surf. Coat. Technol. 2022, 441, 128540.

58. Zhang, P., Liu, S., Lu, Y. Microstructure and interface analysis of Inconel 718 cladding on AISI 304 stainless steel by laser additive manufacturing. J. Manuf. Process. 2020, 56, 312–320.

59. Luo, C., Liu, W., Chen, Y., et al. Effect of interlayer temperature on microstructure and hardness in laser wire deposition of Inconel 718 on steel. Mater. Charact. 2021, 178, 111279.

60. Costa, L., et al. Laser cladding of Inconel 625 on carbon steel: corrosion and wear resistance. Surf. Coat. Technol. 2013, 237, 107–114.

61. Khorrami, M.S., et al. High-temperature performance of Inconel 625 coatings on 304 stainless steel produced by laser metal deposition. J. Mater. Res. Technol. 2021, 14, 2632–2643.

62. Yue, S., Chen, X., Ding, J., Qiu, C. Microstructure and porosity formation mechanisms in laser additive manufactured Inconel 718. J. Mater. Process. Technol. 2018, 254, 259-268.

63. Yan, A.W., Jin, W.L., He, Y.C. Cracking susceptibility and microstructure evolution of Inconel 718 deposited on carbon steel by laser cladding. Mater. Charact. 2018, 137, 78-87.

64. Song, M.F., Chen, Z.C., Liu, W.L. Influence of hydrogen on porosity and microstructure of laser deposited Inconel 718. J. Alloys Compd. 2019, 774, 865–874.

65. Kumar, R., Babu, S. Effect of process parameters on porosity and mechanical properties of laser metal deposited Inconel 718. Mater. Sci. Eng. A 2019, 759, 167–175.

66. Chen, Y., Li, G., Zhang, X. Solidification cracking behavior of Inconel 718 on steel substrate in laser additive manufacturing. Metall. Mater. Trans. A 2018, 49(6), 2537–2546.

67. Wang, H., Liu, X., Fu, Y. Hydrogen-induced cracking in laser-deposited Inconel 718 claddings on S355 steel. Corros. Sci. 2019, 159, 108087.

68. Chen, Y., Li, G., Zhang, Z. Effect of substrate preheating on crack suppression in laser deposited Inconel 718 claddings. J. Alloys Compd. 2018, 745, 292–299.

69. Kumar, R., Babu, S. Surface roughness and microstructural characterization of Inconel 718 claddings produced by laser metal deposition on stainless steel. Surf. Coat. Technol. 2018, 350, 333–342.

70. Li, J., Xu, X., Zhang, Q. Effect of laser cladding parameters on surface quality of Inconel 718 on steel substrates. Opt. Laser Technol. 2019, 113, 140–149.

71. Zhang, M., Yu, W., Luo, Z. Microstructure heterogeneity and mechanical behavior of Inconel 718 laser claddings on carbon steel. Mater. Charact. 2019, 150, 134–142.

72. Yang, S., Chen, L., Zhang, J. Laves and delta phase formation and its influence on mechanical properties of Inconel 718 claddings. Mater. Sci. Eng. A 2020, 770, 138525.

73. Wang, J., Zhao, Y., Wang, C. In-situ thermal monitoring and process control for improved Inconel 718 laser claddings. Addit. Manuf. 2019, 27, 93–102.

74. Sun, M., Wu, X., Zhang, H. Review on defect formation mechanisms and control in wire laser additive manufacturing of Inconel 718. Mater. Sci. Eng. R 2020, 142, 1–21. https://doi.org/10.1016/j.mser.2020.100580

75. Ferreira, A.A., Darabi, R., Sousa, J.P., Cruz, J.M., Reis, A.R., Vieira, M.F. Optimization of Direct Laser Deposition of a Martensitic Steel Powder (Metco 42C) on 42CrMo4 Steel. Metals 2021, 11(4), 672. https://doi.org/10.3390/met11040672

76. Xu, et al. Experimental Studies on the Anisotropic Fatigue Behaviour of IN718 Fabricated via Wire Arc Additive Manufacturing. Metals 2023, 14(7), 770.

77. Ni, et al. Microstructural and Tensile Properties Anisotropy of Additively Manufactured IN718. Materials 2020, 13(21), 4829.